SEVENTH INTERNATIONAL WORKSHOP ON TROPICAL CYCLONES

Topic 1.3   **Air-Sea Interface and Oceanic Influences**

Rapporteur: L. K. (Nick) Shay
                Upper Ocean Dynamics Laboratory
                Division of Meteorology and Physical Oceanography
                Rosenstiel School of Marine and Atmospheric Science
                University of Miami
                4600 Rickenbacker Causeway
                Miami, FL 33149, USA
e-mail: nshay@rsmas.miami.edu
fax: 305-421-4696

Working Group: M. M. Ali, D. Barbary, E. A. D'Asaro, G. Halliwell, J. Doyle, C. Fairall, I. Ginis, I-I Lin, I-J Moon, P. Sandery, E. Uhlhorn, A. Wada

1.3.1: Introduction

The objective of this report is to document progress since IWTC-VI in this thematic area from experimental, observational, empirical, theoretical, and numerical perspectives. The report benefits from the recently published Book Chapter entitled Air-Sea Interactions In Tropical Cyclones (Shay, 2010) in the second edition of the Global Perspectives of Tropical Cyclones edited by Chan and Kepert (2010). The report begins by briefly describing progress in upper-ocean processes that include the oceanic mixed layer (OML) and the thermocline. This section is followed by a discussion of the air-sea interface that includes surface winds and waves, and the communication to the atmospheric boundary layer through the momentum and enthalpy fluxes across the interface. These findings are summarized within a global context with specific recommendations to the WMO's CAS.

1.3.2: Upper-Ocean Response Processes

Coupled oceanic and atmospheric models to predict hurricane intensity and structure change will eventually be used to issue forecasts to the public who increasingly rely on the most advanced weather forecasting systems to prepare for landfall (Marks and Shay 1998). For such models, it has become increasingly clear over the past decade that ocean models will have to include realistic initial conditions to simulate not only the oceanic response to hurricane forcing (Price *et al.* 1994; Sanford *et al*. 1987. 2007; Shay 2001; D'Asaro 2003, Jacob and Shay 2003; D'Asaro *et al.* 2007; Lin *et al*. 2008, 2009; Halliwell *et al.* 2008; Wada *et al.* 2009a; Jaimes and Shay 2009, 2010), but also to simulate the atmospheric response to oceanic forcing (Bender and Ginis 2000; Bao *et al.* 2000; Shay et al. 2000, Hong *et al*. 2000; Walker *et al*. 2005; Lin *et al.* 2008, 2009; Wada and Usui 2007; Wu *et al*. 2007; Sandery et al. 2010; Chen *et al*. 2010).

An important example of this later effect was observed during the passages of hurricanes Katrina, Rita, and Wilma during the 2005 Atlantic Ocean hurricane season. Favorable atmospheric conditions prevailed in the Northwest Caribbean Sea and Gulf of Mexico (GOM) as the Loop Current (LC) extended several hundred kilometers north of the Yucatan Strait. As these storms moved over the deep warm pools, all three hurricanes explosively deepened and were more closely correlated with the ocean heat content (OHC) variations (and deep isotherms) than with the sea-surface temperatures (SST) distributions, which were essentially flat and exceeded $30^{o}C$ over most of the region. By contrast, the OHC and $26^{o}C$ isotherm depths indicated the LC and its deep warm layers as it was in the process of shedding a mesoscale warm core ring (WCR) in August and September 2005. A cold core ring (CCR) that advected cyclonically around the shed WCR may have helped weaken Rita before landfall. Walker *et al.* (2005) also found that Hurricane Ivan may have encountered a CCR prior to landfall. These studies point to the importance of initializing coupled models with realistic warm and cold ocean features in the global oceans (Ali *et al.* 2007; Lin *et al*. 2008; 2009; Halliwell *et al.* 2008; 2010 Wada and Ursi 2007; Chen *et al*. 2010; Sandery *et al.* 2010; Zheng et al. 2010).
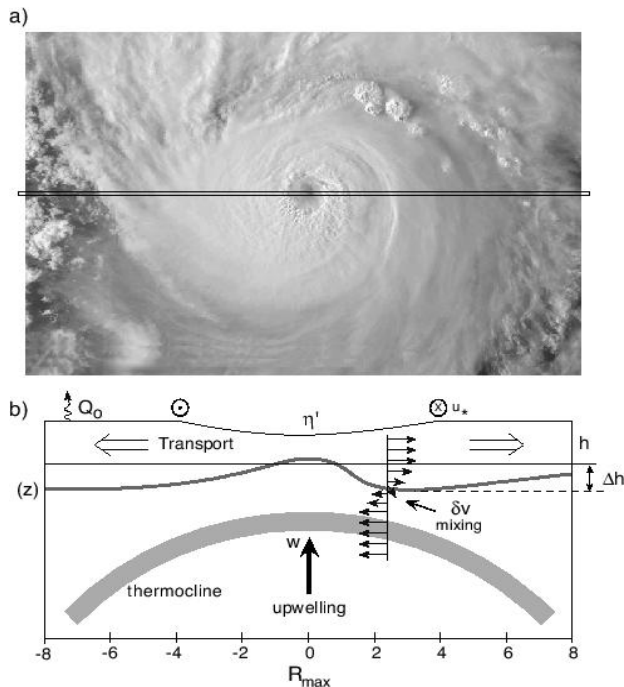

Figure 1 a) Tropical cyclone image and b) schematic of the physical processes forced by hurricane winds such as shear-induced mixing and OML deepening, upwelling due to transport away from the center, and surface heat fluxes from the ocean to the atmosphere, all of which may contribute to ocean cooling during TC passage (from Shay 2009).

As shown in Fig. 1, upper-ocean mixing and cooling are a strong function of forced near-inertial current shears that reduce the Richardson numbers below criticality, which induces entrainment mixing (Price 1981; Schade and Emanuel 1999; Shay 2001; D'Asaro 2003; Jacob and Shay 2003). The contributions to the heat and mass budgets by shear-driven entrainment heat fluxes across the ocean mixed layer (OML) base are 60 to 85%, surface heat fluxes are between 5 to 15%, and horizontal advection by ocean currents are 5 to 15 % (Price *et al.* 1994; Jacob *et al.* 2000). All of these processes impact the SST and OHC variability. In addition, wind-driven upwelling of the isotherms due to net upper ocean transport away from the storm modulate the shear-induced (S) ocean mixing events by an

upward transport of cooler water from the thermocline. This transport increases the buoyancy frequency (N), which tends to keep the Richardson number above criticality. In the LC and WCR regimes with deep, warm thermal layers, cooling induced by these physical processes (Fig. 1) is considerably less as much greater turbulent-induced mixing by the current shear is required to cool and deepen the OML (Shay and Uhlhorn 2008). Quantifying the effects of forced current (and shear) on the OHC and SST distributions is central to accurately forecasting hurricane intensity and structure change.

1.3.2.1 Oceanic Thermal Response

Walker *et al.* (2005) showed that the SST response was modulated by both WCR and CCR in the Gulf of Mexico during Ivan's passage (Fig. 2). Up to 7°C cooling was observed in the CCR due in part to upwelling associated with TC Ivan's wind stress curl. Upward isotherm displacements of up to 65 m were documented from altimeter-derived surface height anomaly (SHA) and wind stress curl. This result was corroborated using a reduced-gravity model where for each 10 cm surface height change, the isotherm displacement is approximately 33 m. The observed 20 cm decrease in the SHA field may have been associated with the barotropic (sea-surface) trough in the cooling wake (Geisler 1970; Shay and Chang 1997). While this depressed sea surface and the SST cooling provided *negative feedback* to Ivan, the associated phytoplankton blooms in the wake had peak concentrations of chlorophyll A (Chl-a) exceeding 1 mg m^{-3} distributed over 13,000 km^{2} area detected from SeaWIFS imagery compared to background concentrations of less than 0.5 mg m^{-3}. This relative maximum occurred about 3 to 4 days following passage in the vicinity of the CCR. By contrast, the SSTs in the WCR only decreased by 1 to 2°C during Ivan, consistent with previous studies.

In the wake of TC Ketsana (Oct 2003) in the western Pacific ocean basin, SST imagery by the Advanced Microwave Sounding Radiometer (AMSR) and chlorophyll concentrations from the Moderate Resolution Imaging Spectro-radiometer (MODIS) were combined to assess the oceanic response (Yin *et al.* 2007). Based on post-storm measurements, Chl-a concentrations increased to1.2 mg m^{-3} about 7 days after passage. This equates to more than an order of magnitude change induced by upwelling of nutrients from the cooler thermocline water. The maximum Chl-a level found was more than 3 mg m^{-3} in Ketsana's cold wake as this response persisted for more than two weeks following TC passage. Simulations using a Regional Ocean Modeling System with a Nitrogen-Phytoplanton-Zooplankton-Detritus (NPZD) biochemical model revealed levels of Chl-a of 0.4 to 1.7 mg m^{-3}, consistent with satellite estimates. The typhoon's wind stress curl induced significant upwelling into the OML and forced this large phytoplankton bloom. These results are in agreement with Walker *et al.* (2005) and Hanshaw *et al.* (2008).

Park *et al.* (2005) combined ARGO float temperature and salinity profiles with satellite-derived SSTs to document the thermal response to typhoons in the western Pacific Ocean (WPAC) over ten-day periods (Fig. 3). They found a high correlation of OML temperature

changes and SSTs, but there was a strong dependence on latitude and initial OML depth. A key result was a negative correlation between OML depth change and its initial depth that
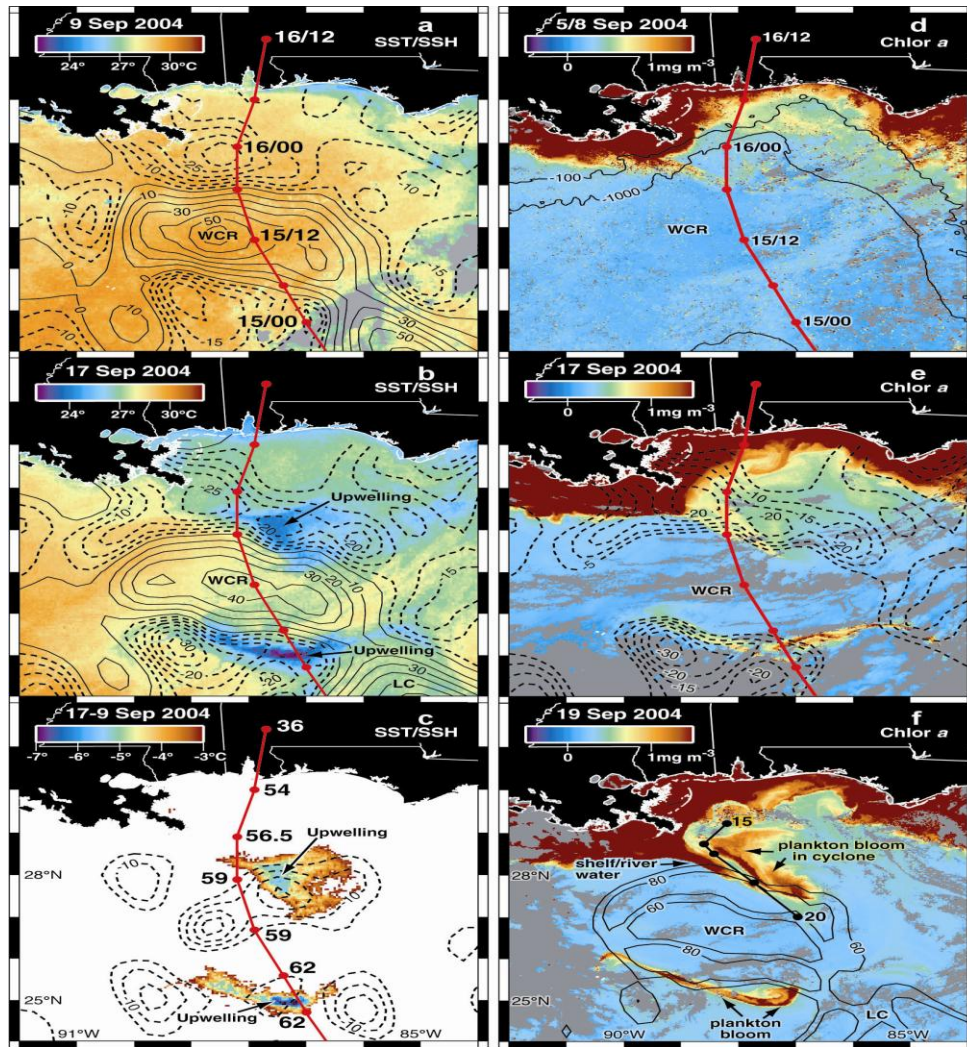

Fig. 2: SSTs (color: ^{o}C) and SHA's (contours: cm) a) pre (9 Sept) and b) post Ivan (17 Sept) and c) SST and SHA differences where wind speeds from Ivan are shown in m s^{-1} and Chlorophyll a (mg m^{-3}: right panels) corresponding to similar days for d) pre, e) post and f) 19 Sept for corresponding isotachs derived from the SHA gradients (Combined from Figs 2 and 3 in Walker *et al.* 2005).

exceeded 50 m (a proxy for the Kuroshio's location and its WCR field). In the Kuroshio Current, the OML depth changes are less where the SST cooled by 1 to 2°C. This result has consequences for both the genesis and the development of a mature typhoon. This result underscores the inherent oceanic variability in the vicinity of western boundary

currents and their background eddy fields. Strong gradients in the OML depths and temperatures play a pivotal role in TC intensity changes discussed below.
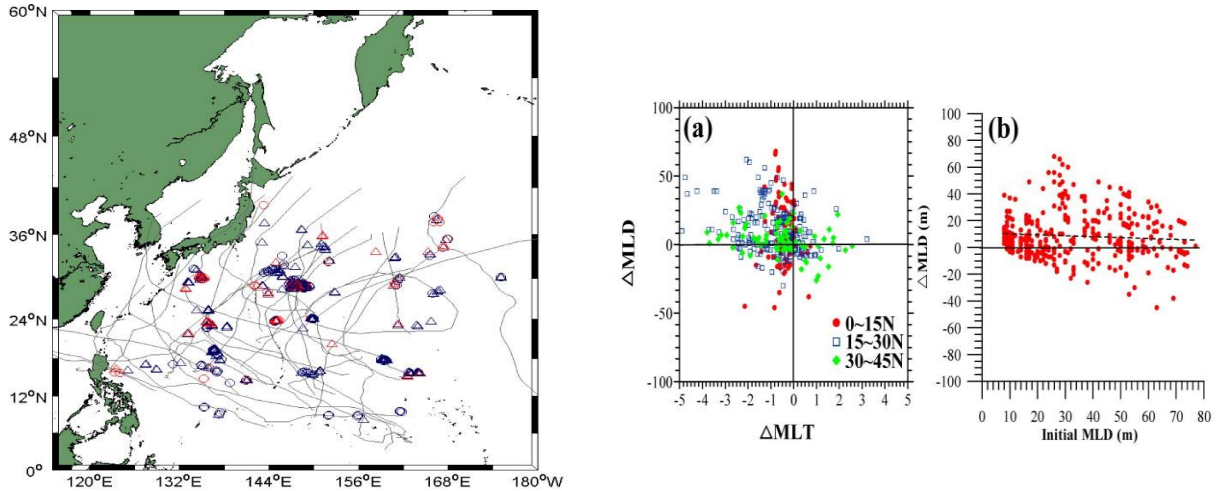

Figure 3: Distribution of typhoon tracks (left panel) relative to the ARGO float pairs in the Western Pacific Ocean from 1999-2003 and scatter (right panels) for a) OML temperature change (ΔMLT: ^{o}C) and depth change (ΔMLD : m) binned by bands (red: 0-15°N; blue 15-30°N; green: 30-45°N) and b) initial depth (MLD : m) and depth change (ΔMLD : m) (From Park *et al.* 2005).

During the ONR-CBLAST (2004), technology for measuring the ocean response to tropical cyclones using air-deployed instrumentation was advanced. Several varieties of floats and surface drifters were deployed into Hurricane Frances (2004) and measured temperature, salinity and velocity response of the ocean to the storm (Black *et al.* 2007; D'Asaro *et al.,* 2007; Sanford *et al.* 2007). As shown in Fig. 4, profiler data are sufficient to resolve the SST response where the cold wake with maximum cooling of 2.2^{o}C is clearly offset from both the center of the storm and from the strongest winds. Less cooling occurred on the left-hand side of the storm (0.8^{o}C) and under the central core (0.4^{o}C). Accordingly, the reduction in air-sea heat flux in the core due to this cooling is modest, only about 16%. The upper layer velocity (Fig. 1.3.4a, arrows) is also largest in the cold wake, reaching 1.6 m s^{-1}, consistent with the cold wake being formed by near-inertially resonant, shear-driven mixing (Price 1981). The changes in the depth of the 24°C isotherm (Fig. 4b) differ from SST. Currents are weak and upwelling of up to 50 m occurs only behind the storm with weak downwelling, typically 10 m at large distances from the eye. Temporal variations in currents and isotherm depth occur at nearly the inertial period with a pattern of phase propagation suggestive of the propagation of near-inertial waves downward and away from the storm. The ocean heat change (Fig. 4c) reflects the patterns of both SST and isotherm depth with low values behind the eye due to upwelling which periodically reverses as the upwelling is replaced by downwelling over the inertial cycle. A more detailed analysis of these data show that the heat varies both spatially and temporally

as the oscillating vertical and horizontal currents advect heat in three dimensions, consistent with previous studies. These Lagrangian technologies when complemented with aircraft based measurements from synoptic grids (Eulerian) increase our ability to measure the oceanic parts of the TC system with the same resolution and accuracy as the atmospheric part.
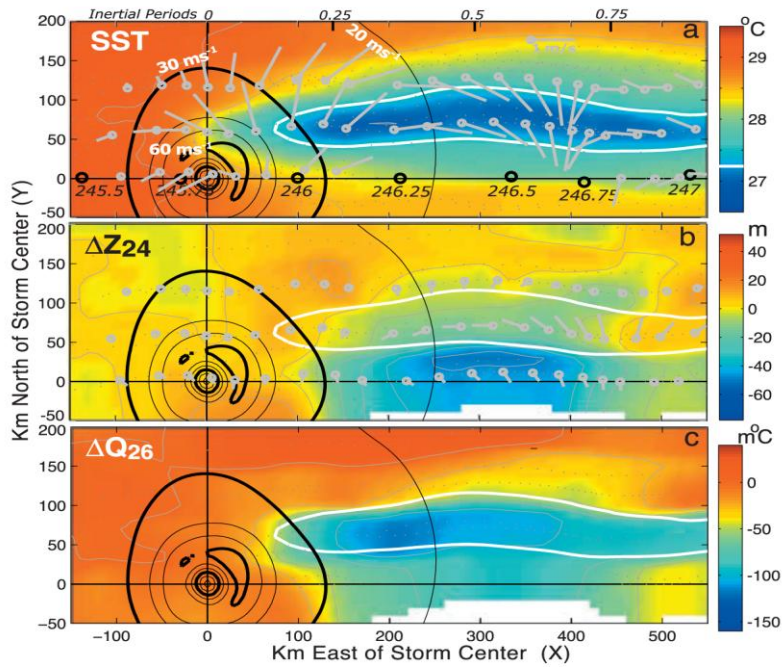

Fig. 4. Plan view of Hurricane Frances (2004) response in a storm centered coordinate system where the storm moved towards the left along the x-axis. Wind speed contours (black, white contours) are derived from HWIND (Powell and Houston 1996) on yearday 245.75. a) SST from both drifters and floats where dots represent the data points; colors and contours show the mapped field. Arrows depict the mixed layer currents from EM-APEX floats; b) Change in the depth of the 24°C isotherm from its value on yearday 245.6 and the current along this isotherm; and c) change in the heat warmer than 26°C. Data in panels b and c are from floats only (from D'Asaro *et al.* 2007).

1.3.2.1 Oceanic Current Response

Observations of the ocean current response to TC passage have been generally sparse over the global oceans as the community has had to rely on fortuitous encounters with buoys and moorings deployed in support of other experiments or ships crossing TC wakes (Shay and Elsberry 1987; Church *et al.* 1986; Teague *et al.* 2007, Zedler *et al.* 2001). Using a network of high frequency radar stations (Yoshikawa *et al.* 2006), a strong wind-driven current response was observed during typhoon Mari's passage in the Tsushima Strait. Surface currents have also been shown to impact the direction of the surface wind stress (Drennan and Shay 2006). The divergent surface velocity response exceeded 50 cm s^{-1},

which is indicative of a 3-D response and upwelling processes (Yablonsky and Ginis 2009; Halliwell *et al*. 2010). Wind-forced currents directly affect the thermal, haline and mass field response to TC passage. Recent airborne field experiments to measure the momentum and thermal response during TC passage are listed in Table 1.

TC	Basin	Year	Instrument(s)	References
Norbert	EPAC	1984	AXCP	Sanford *et al.* (1987)
Josephine	WATL	1984	AXCP	Sanford *et al.* (1987)
Gloria	WATL	1985	AXCP Drifters	Black *et al.* (1988); Price *et al.* (1994)
Gilbert	GOM	1988	AXCP	Shay *et al.* (1992)
Dennis	WATL	1998	Floats	D'Asaro (2003)
Isidore /Lili	GOM	2002	AXCP AXCTD	Shay and Uhlhorn (2008)
Frances	WATL	2004	EMAPEX floats	Sanford *et al.* (2007); D'Asaro et al. (2007)
Katrina/Rita	GOM	2005	AXCTD AXCP	Jaimes and Shay (2009)
Gustav	GOM	2008	EMAPEX floats	

Table 1: Summary of aircraft field programs where currents and shears were observed during TC passage where EPAC-Eastern Pacific Ocean, WATL-Western Atlantic Ocean, GOM-Gulf of Mexico, AXCP-airborne expendable current profiler, AXCTD- airborne expendable conductivity temperature and depth profiler, EMAPEX-ElectroMagnetic Autonomous Profiling Experimental Floats.

One clear example of a fortuitous encounter occurred during TC Ivan (2004) over an array of moored Acoustic Doppler Current Profilers (ADCP) as shown in Fig. 5. Fourteen moorings were deployed about 180 km south of Mobile, Alabama as part of the Slope to Shelf Energetics and Exchange Dynamics (SEED) project from early May through early Nov 2004. During the period of deployment TC Ivan passed directly over these ADCP moorings (Teague *et al.* 2006, 2007), which provided the temporal evolution of the 3-D current (and shear) structure at 2 to 4-m vertical resolution. The response at Ivan moorings is shown in Fig. 6 for the near-inertial wave band where the local IP is ~24 h at 30°N. Profiler data started at a depth of 50 m and extended to 500 m at 4-m intervals. Shay (2009) found amplitudes of 4 to 6 cm s^{-1} in agreement with those determined from limited vertical sampling from the Hurricane Frederic current meter arrays in the DeSoto Canyon area (Shay and Chang 1997). These barotropic current signals have large phase speeds and are associated with Poincare' wave motions (e.g., long waves with rotation).
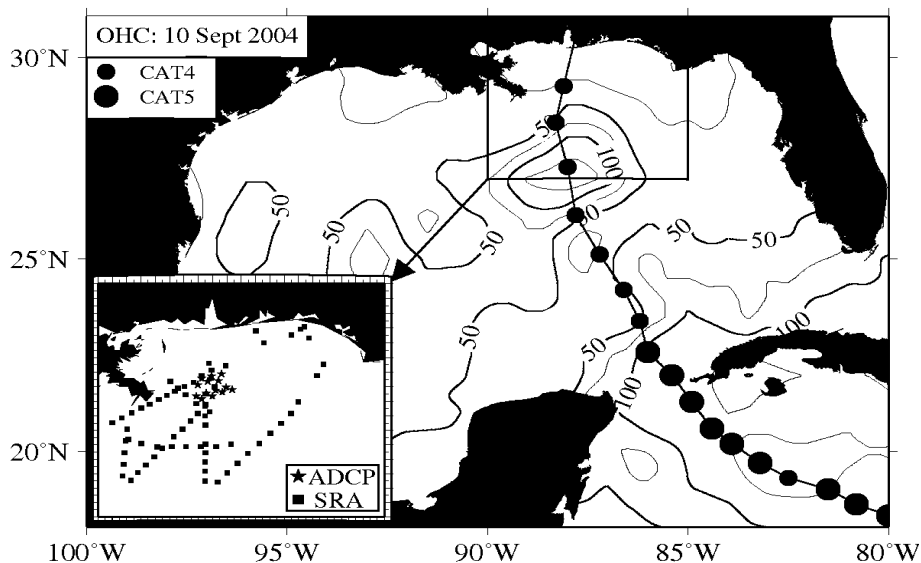
Fig. 5: OHC map (contours are kJ cm^{-2}) and inset showing NRL mooring locations (stars) and scanning radar altimeter directional wave measurements (Wright *et al.* 2001: squares) relative to Ivan's track and intensity. The OHC pattern shows the WCR encountered by Ivan prior to landfall. The cooler shelf water (OHC < 20 KJ cm^{-2}) resulted from TC Frances two weeks earlier.

Profiles at 1.5 Rmax to the right of Ivan's track indicate a clear downward propagation of the baroclinic energy (V_g) from the wind-forced OML current into the thermocline, consistent with an upward propagating phase velocity (V_p). Baroclinic motions, which are the most energetic part of the ocean's momentum response to a moving TC, have a characteristic time scale for the phase of each mode to separate from the OML current structure when the wind stress scale ($2R_{max}$) exceeds the deformation radius of the first baroclinic mode (~ 30 to 40 km) (Gill 1984). This time scale increases with mode number due to decreasing phase speeds (Shay 2009). This vertical propagation is primarily associated with the predominance of the anticyclonic-rotating (clockwise in northern hemisphere) energy (Shay and Jacob 2006) From measurements, the ratio of the anticyclonic to cyclonic energies range from values of 3 to 4, indicative of a preference for downward energy propagation from the OML. The corresponding vertical energy flux indicated an average value of ~2 ergs cm^{-2} s^{-1}. This energy flux is similar to that estimated from near-inertial current profiles deployed in a frontal regime by Kunze and Sanford (1985). This result suggests that TCs are as effective as fronts in transferring wind-forced energy into the thermocline.
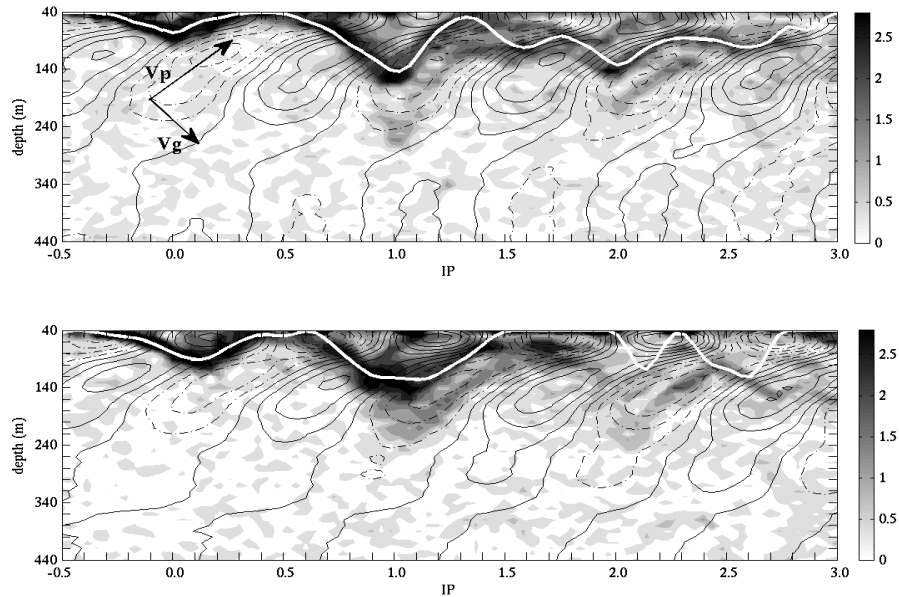
Fig. 6: Band-pass filtered cross-track current structure along the track (upper panel) and at 1.5R_{max} (lower panel) contoured at 5 cm s^{-1} with t = 0 the time of TC Ivan's passage and the time axis normalized by the inertial period (~1 day). Heavy solid line represents the depth of the magnitude of the maximum shear (gray shade x 10^2 s^{-1}). Arrows represent upward phase (**Vp**) with downward group velocity (**Vg**) indicative of downward propagating waves into the thermocline. Time interval spans 15-19 Sept (Data courtesy Naval Research Laboratory).

As noted, near-inertial current shears are central to the oceanic cooling by lowering the bulk (gradient) Richardson numbers to < 1 (0.25) and forcing the OML to deepen through instabilities. Uhlhorn (2008) documented the magnitude of the observed current shears range from several experiments listed in Table 1. A value of 1.4 x 10^{-2} s^{-1} was found from TC Lili measurements in the LC to as high as 3.5 x 10^{-2} s^{-1} in the GCW during TC Gilbert. In the regime influenced by TC Ivan with relatively shallow OML, the shear is nearly three times larger than that observed in the LC system (Shay and Uhlhorn 2008). Higher vertical shear levels were observed from the EM/APEX floats deployed in TC Frances (Sanford *et al.* 2005; 2007). As shown in Fig. 7, higher shear levels forced mixing events during Frances passage by essentially lowering the gradient Richardson number to below 0.25 (S^2 − $4N^2$ > 0) across the base of the OML at 1 to 2Rmax to the right of the track. During this period of intense forcing, strong near-inertial currents were excited by the TC of up to 1.6 m s^{-1} which created the vigorous shears (Sanford *et al.* 2007). Cooling level in TC Frances was ≈ 2.2 ^{o}C as shown above (D'Asaro *et al.* 2007).
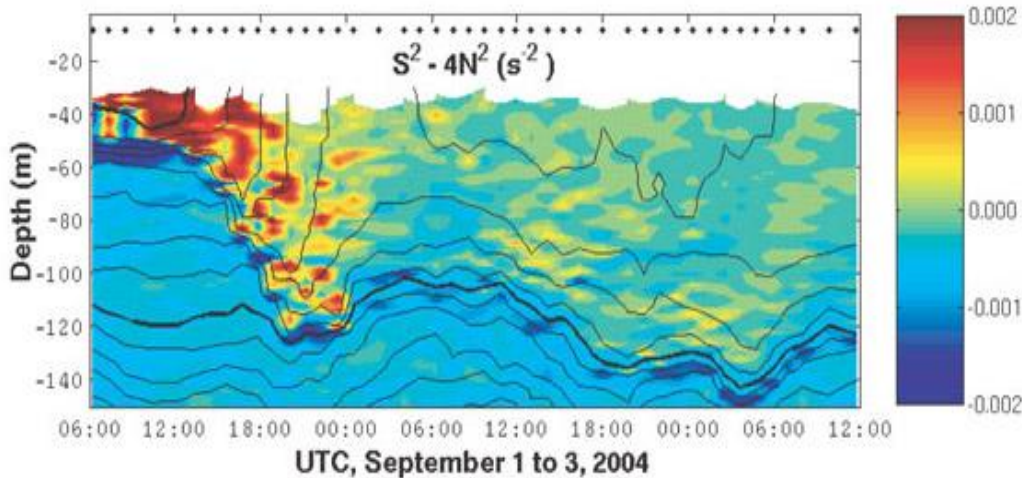
Fig. 7: Reduced shear (color: s^{-2}) based on the gradient Richardson (Ri = N^2 S^{-2} where N is the buoyancy frequency and S is the shear) and the temperature (contours: ^{o}C) contoured at 0.5^{o}C intervals number where the heavy black contours represent 29 and 25°C during and subsequent to Frances. The shear instability criterion is simply rewritten as S^2 – 4N^2 >0 to represent mixing events (values greater than 0) in yellow and red. Blue colors represent stable conditions. Analysis is based on data from one EM/APEX float described in Sanford *et al.* (2005; 2007). The time of closest approach of TC Frances at 1700 UTC 1 Sept 2004.

1.3.3: Oceanic Background States and Parameterizations

1.3.3.1 Background Ocean States

Background oceanic flows that are set up by large horizontal pressure gradients due to T(z) and S(z) may play a significant role in altering the development of strong wind-driven current shears within the LC/WCR complex as suggested in Fig. 8 (Shay and Uhlhorn 2008). Pre- and post-Isidore measurements across the Yucatan Strait indicate strong density and pressure gradients that are associated with the northward-flowing LC at speeds of up to 1 m s^{-1}. In the post-Isidore case, the horizontal gradients were sharpened since the storm cooled the Yucatan shelf waters by more than 4°C compared to less than 1°C across the Yucatan Strait. Here, strong horizontal advection of the thermal and salinity gradients through this regime impacted the oceanic response within the LC. Falkovich et al. (2005) introduced an approach for feature-based ocean modeling that involves cross-frontal "sharpening" of the background temperature and salinity fields according to data obtained in field experiments, which allows specifying the position of the LC in the GOM using available observations.

Briefly, the LC is a highly variable ocean feature in time as it can penetrate ~500 km northward of the Yucatan Strait. Recurring WCR shedding events with peak periods from 6 to 11 months (Sturges and Leben 2000) occur when CCRs are located on the LC

periphery prior to separation. These WCRs, with diameters of ~200 km, propagate west to southwest at phase speeds of 3 to 5 km d^{-1} (Elliot 1982), and can remain in the Gulf of Mexico for several months. In this LC regime, OHC values relative to the 26°C isotherm exceed 100 kJ cm^{-2} (Leipper and Volgenau 1972). Such OHC levels are resistive to storm-induced cooling by wind-driven current shears across the OML base.
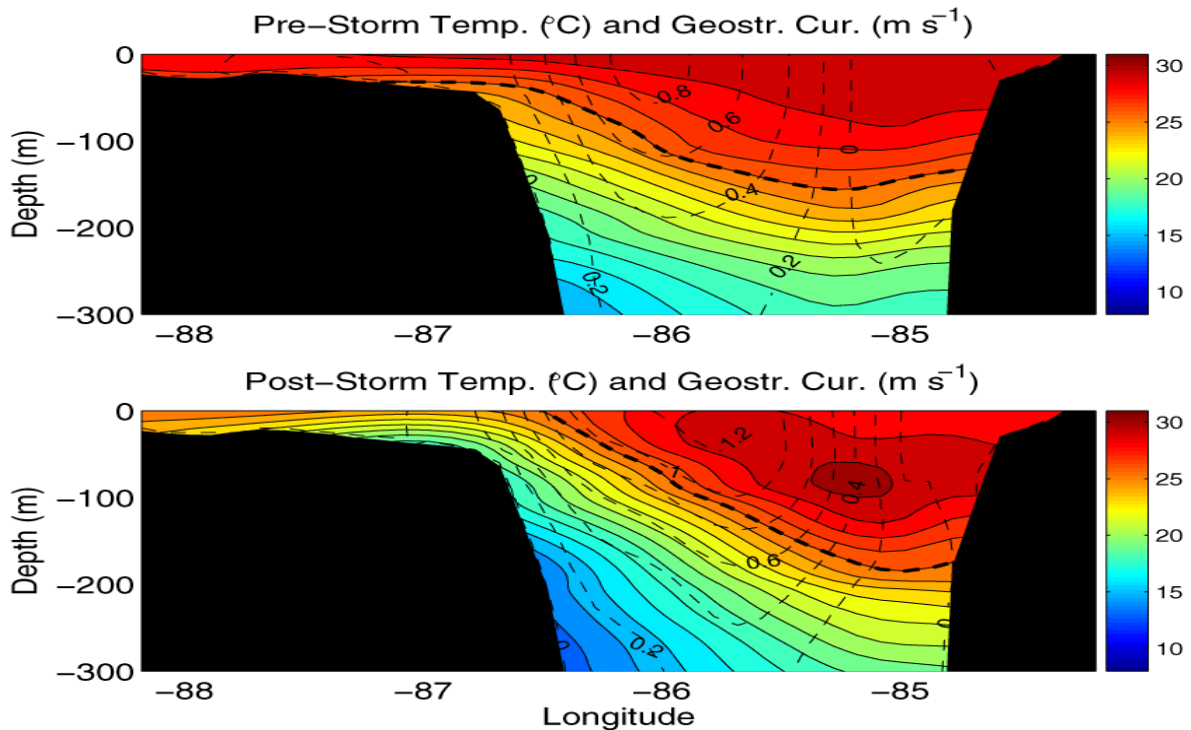

Fig. 8: Pre-(upper) and post-Isidore (lower) thermal (^{o}C: color) and northward (into the page) geostrophic velocity (m s^{-1}: dashed) cross-section from expendables deployed on 19 and 23 September 2002 across the Yucatan Straits. Heavy dashed line represents the 26°C isotherm depth (from Shay and Uhlhorn 2008).

Data assimilative ocean nowcasts are an effective method for providing initial and boundary conditions to the ocean component of nested, coupled TC prediction models. The thermal energy available to intensify and maintain a TC depends on both the temperature and thickness of the upper ocean warm layer. The ocean model must be initialized so that ocean features associated with relatively large or small OHC values are in the correct locations and T-S (and density) profiles, along with the OHC, are realistic. Ocean nowcast-forecast systems based on HYCOM (Chassignet *et al.* 2003; Halliwell 2004) were evaluated in the northwest Caribbean and eastern Gulf of Mexico for September 2002 prior to Hurricanes Isidore and Lili, and for Sept. 2004 prior to Hurricane Ivan. In this region, the OHC distribution associated with the LC/WCR complex as well as coastal upwelling must be accurately initialized for the ocean model. In this context, measurements are

critically important not only for assimilation, but to evaluate initial and boundary ocean fields.
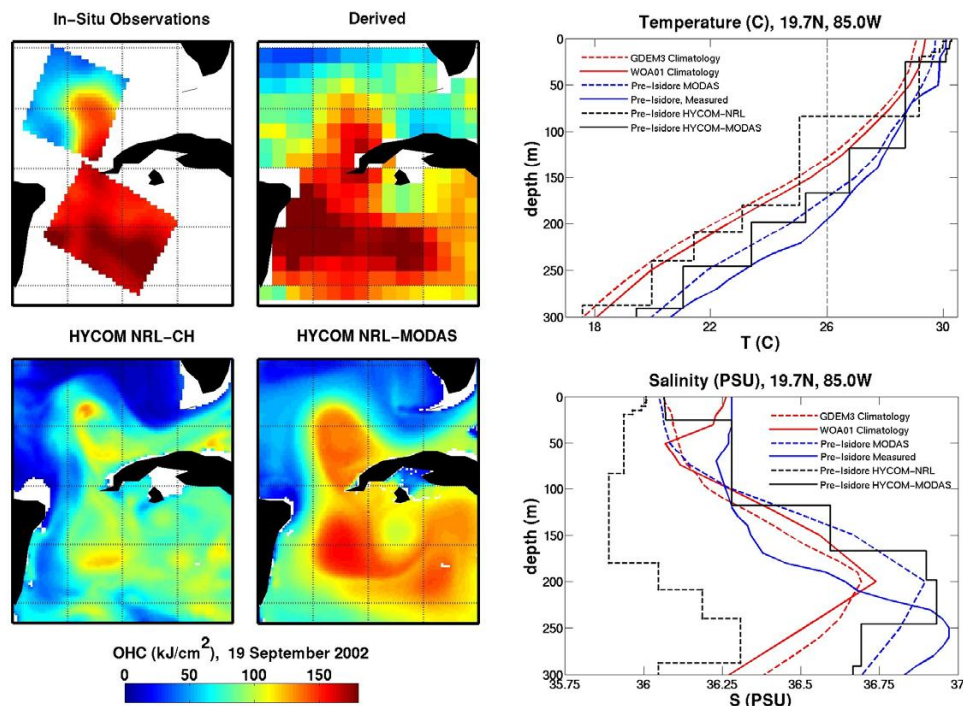

Fig. 9: OHC (kJ cm^{-2}) in the northwest Caribbean Sea and southeast GOM from an objective analysis of aircraft observations, satellite altimetry, HYCOM NRL-CH nowcast, and HYCOM NRL-MODAS nowcast (four left panels). Temperature (right top) and salinity (right bottom) vertical profiles at a location in the northwest Caribbean Sea, where red lines are climatological profiles (GDEM3 dashed, WOA01 solid), solid blue lines are observed profiles, dashed blue lines are MODAS profiles, and black lines are model nowcasts (HYCOM-NRL dashed; HYCOM-MODAS solid) (From Halliwell *et al.* 2008).

An examination of the initial analysis prior to Isidore is from the experimental HYCOM nowcast-forecast system of the NRL experiments in the Atlantic basin at 0.08° resolution. This model product assimilates both satellite altimetry SHAs (Cooper and Haines 1996) and optimally interpolated SSTs. Comparison of OHC maps hindcast by HYCOM to OHC maps objectively analyzed from aircraft measurements and derived from satellite observations (left panels of Fig. 9) demonstrate that this HYCOM analysis (labeled HYCOM NRL-CH in the figure) reproduces the LC orientation but underestimates OHC. In the NW Caribbean Sea, the T(z) hindcast tends to follow the September climatology but does not reproduce the larger OHC values. In the HYCOM hindcast, the upper ocean is less saline than both climatology and observations above 250 m and less saline than the observations between 250 and 500 m. HYCOM structure was subsequently relaxed to the Navy three-dimensional MODAS (Fox *et al.* 2002) and T-S analyses were generated from

all available *in-situ* observations. The first HYCOM NRL-CH nowcast was adversely impacted by a poor initialization that could not be corrected by including only the SHA fields. Biases were reduced in this HYCOM NRL-MODAS product compared to observations in both horizontal maps and vertical profiles. Evaluation of the next-generation NRL nowcast-forecast system (Cummings 2003) is being done by performing hindcasts from mid-2003 to the present for Ivan (2004) and Katrina and Rita (2005). Initial evaluation of pre-Ivan conditions is encouraging because the large cold bias was no longer present, and because the LC/WCR complex (includes the CCR) was well represented (see Fig. 2).

1.3.3.2 Vertical Mixing Parameterization

One of the significant effects on the upper-ocean heat budget and the fluxes to the atmosphere is the choice of entrainment mixing parameterizations (Jacob *et al.* 2000; Wada *et al.* 2009a; Halliwell *et al.* 2010). Jacob *et al.* (2000) and more recently Halliwell *et al.* (2010) have conducted sensitivity tests using five schemes: K-Profile Parameterization (KPP: Large et al. 1994); Goddard Institute for Space Studies Level-2 closure (GISS: Canuto et al. 2002); Level-2.5 turbulence closure scheme (MY: Mellor and Yamada, 1982); quasi-slab dynamical instability model (PWP: Price et al. 1986); and the turbulent balance model of Gaspar (KT: 1988) that is a modified version of Kraus and Turner (1967). For quiescent ocean initial conditions, the range of fluxes in the directly forced region of Hurricane Gilbert exceeds 500 Wm^{-2} for these five schemes.

For the Hurricane Gilbert case, Jacob and Shay (2003) found that the three higher-order turbulent mixing schemes (KPP, MY, GISS) lead to a more accurate ocean response simulation based on comparisons to the *in-situ* measurements. Halliwell *et al.* (2010) conducted a series of sensitivity tests using the Hurricane Ivan data as a guide to understand the impact of both surface drag coefficients and vertical mixing parameterizations in HYCOM. They directly compared both the current and current shears measured at one of the moorings located about 1.5 Rmax to the right of the track. Of particular interest, the shear magnitudes revealed very high correlations with the HYCOM model using the KPP mixing scheme with the Donelan *et al.* drag coefficient over the first two inertial periods (Fig. 10). Shear comparisons reveal differences among the three vertical mixing schemes evaluated in KPP, MY and GISS as well as the surface drag coefficient parameterizations of Donelan *et al*., Powell *et al*. and Large and Pond. Donelan *et al*. c_d seems to produce the most realistic shear profile in the upper 150 m compared to the Powell et al. and the Large and Pond formulations. Based on these comparisons, KPP mixing scheme with the Donelan drag coefficient are the schemes of choice for the Ivan data set. We are in the process of making such comparisons for all the ADCP records during storm forcing period. The import of this surface drag coefficient parameterization and surface stress drives the current and its shear that will lead to enhanced shear instabilities and entrainment mixing. So these schemes are clearly linked in obvious and subtle ways to fluxes and TC intensity change (Halliwell *et al.* 2010).
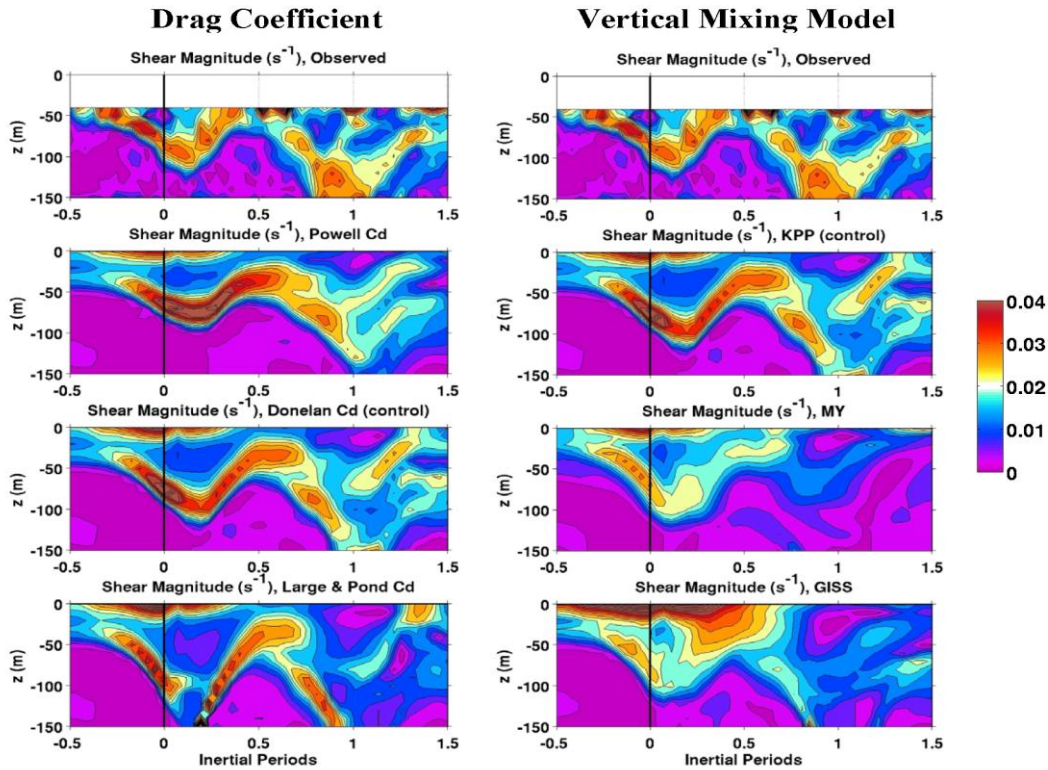
Fig. 10: Time series of the magnitude of vertical current shear (s⁻¹) comparing observations from SEED mooring 9 (upper panels) to three wind stress drag coefficient choices (left) and vertical mixing choices (right) over two inertial periods. The black line represents the time of Ivan's closest approach to.the mooring (t=0). The combination of KPP mixing scheme and Donelan *et al.* drag coefficient parameterization produce the most realistic shear structure and maximum OML depth relative to the data. Note that the quality ADCP data started at about 40 m which avoids surface interference effects.

The OML salinity evolution with and without precipitation forcing highlights the effect of precipitation on the upper ocean salt budget (Jacob and Koblinsky 2007). For the no precipitation case, OML salinity variability simulated by all the above mixing schemes was similar ahead of the storm center. In the PWP scheme, however, salinity increases significantly in the right-rear quadrant over the first half of an inertial period due to due to enhanced mixing. While in the other mixing cases, the simulated salinity evolution is similar with minimal changes in the KT model due to less intense mixing (no vertical shear). By including precipitation forcing, the salinity in the OML began to decrease about 0.5 IP before the storm with maximum freshening of the OML observed in the KT case. This freshening process due to enhanced precipitation increases static stability in the mixed layer, leading to a simulated salinity balance for PWP case that is more consistent with the other schemes. OML temperature and salinity evolution in cases with and without precipitation for PWP scheme indicates a mean temperature and salinity differences of

0.5°C and 0.2 psu in the OML layer. An average freshening of 0.2 psu is seen in the wake of the storm in all the five cases when precipitation forcing was used, which is consistent with CTD measurements acquired during the Spectrum 90 expeditions (Pudov and Petrichenko 2000). Precipitation temperatures have minimal effect on the salinity evolution in the OML. Simulated results from the three-higher order schemes did not differ significantly from each other.

These comparisons are limited by data availability and therefore routine measurements are necessary to evaluate the ocean component of the coupled system. Similar to the post-season track and intensity verifications, more ocean observations (including current and salinity) must be acquired to evaluate the different schemes to build a larger statistical base. The approach of stand-alone ocean simulations using derived realistic atmospheric forcing used here allows us to evaluate the ocean model and associated parameterizations. Since boundary layer forcing structure from the atmospheric component of the coupled model is subject to additional uncertainties, this approach will eventually lead to reduction in uncertainties of the ocean component in the coupled system driven by observations.

1.3.3.3 Oceanic Heat Content Estimates

If the upper-ocean warm layer is thick and has a large total OHC, the SST will decrease slowly during TC passage, the negative feedback mechanism (or "brake") will be weak, and the ocean will promote TC intensification. Several studies over the globe have now shown that OHC relative to the depth of the $26°C$ isotherm takes this into account and is a better indicator than a thin layer of high SST on TC intensification. Leipper and Volgenau (1972) estimated OHC as:

$$\text{OHC} = c_p \int_0^{D26} \rho \left[T\left(z\right) - 26 \right] \, dz,$$

where c_p is specific heat at constant pressure (1 cal gm^{-1} $°C^{-1}$), D26 is the 26°C isotherm depth, and OHC is zero wherever water above 26°C is not present. It is difficult to monitor the global oceans for isotherm depths, thermal structure and OHC given the relative paucity of *in situ* profiler measurements with perhaps the exception of the global ARGO float network. Thus, satellite remote sensing offers the optimal approach to infer isotherm depths and OHC variations . Measurements from radar altimeter missions (Fig. 11) of the SHA field from NASA TOPEX, Jason-1 and Jason-2,   U.S. Navy Geosat Follow-On-Mission (GFO), Envisat and ERS-2 (Cheney *et al.* 1994; Scharroo *et al.* 2005) and SSTs are used in a reduced gravity model (e.g., Goni *et al.* 1996) with hurricane season climatology (Mainelli et al. 2008). Since mesoscale ocean features only move a few km d^{-1}, altimeter-derived SHA locates warm (cold) features that are usually identified as positive (negative) values as observed during TC's Opal (Shay *et al.* 2000), Ivan (Walker *et al.* 2005; Halliwell *et al.* 2008), Katrina and Rita in the Gulf of Mexico (Mainelli *et al.* 2008 ; Jaimes and Shay 2009), Maemi (Lin *et al.* 2005,2008, 2009; Wu *et al.* 2007), Chaba and

Songda (Wada and Usui 2007) in the western Pacific Ocean basin, and cyclones in the Bay of Bengal (Jena *et al.* 2006; Ali *et al.* 2007).
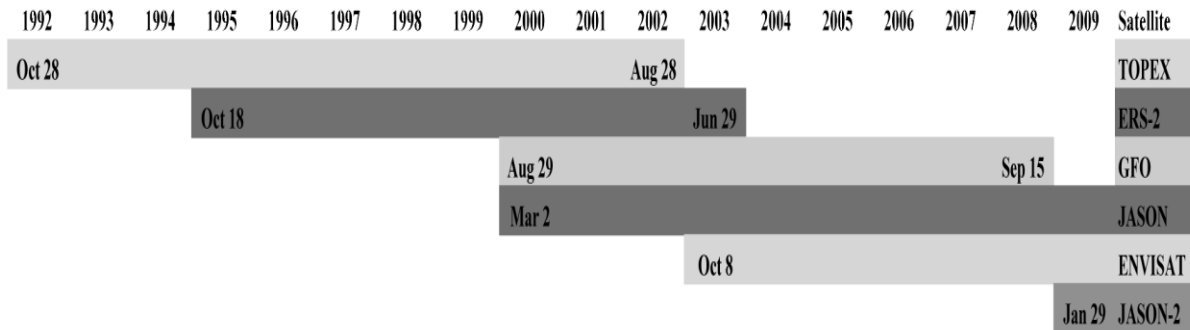

Fig. 11: Bar chart showing time line of available SHA field from various altimetry platforms.

Lin *et al.* (2005) point out the importance of the eddy-rich regime associated with the western boundary current or Kuroshio during the passage of typhoons over these oceanic features. In the western Pacific Ocean, the Kuroshio plays the same role as the Gulf Stream in the western Atlantic Ocean basin (i.e., poleward advection of warm tropical water). Using 13 years' of satellite altimetry data, *in situ* Argo float subsurface ocean profiles, and a series of OML numerical experiments, Lin *et al.* (2008) found that the warm ocean eddies in the southern eddy-rich-zone of the Western North Pacific Ocean represent 'boosters' for super–typhoons (Fig. 12). These warm mesoscale ocean eddies can provide much deeper subsurface warm layer and higher OHC. Thus, a TC's self-induced ocean cooling negative feedback to intensification can be effectively restrained and there can be sufficient air-sea enthalpy fluxes available for intensification to the supertyphoon intensity at category-5. Related theoretical work on using coupled typhoon-ocean model to explore the role warm ocean eddies on cyclone intensity (Wu *et al.* 2007). Lin *et al.* (2009a) subsequently found that faster-moving typhoons can afford to intensify to the supertyphoon intensity at category-5 over relatively shallower layer of subsurface warm water (lower OHC) while slower-moving typhoons require much deeper subsurface warm layer (higher OHC) for intensification to category-5. In Lin *et al.* (2009b), a new method was proposed to quantitatively estimate the required minimum upper OHC and depth of the 26°C isotherm for intensification to category-5 intensity according to the translation speeds. This is not surprising since *the time available for vertical mixing* increases (Greatbatch 1983) with slower moving storms. It is also a function of latitude and the strength of the underlying stratification.

Wada and Chan (2008) found that the OHC (or tropical cyclone heat potential TCHP) relative to 26 ^{o}C isotherm depth was high (Fig. 13). The high TCHP area corresponded to the region where TCs underwent rapid intensification (Wang and Zhou 2008). The Empirical Orthogonal Function (EOF) analysis showed three significant TCHP variations:
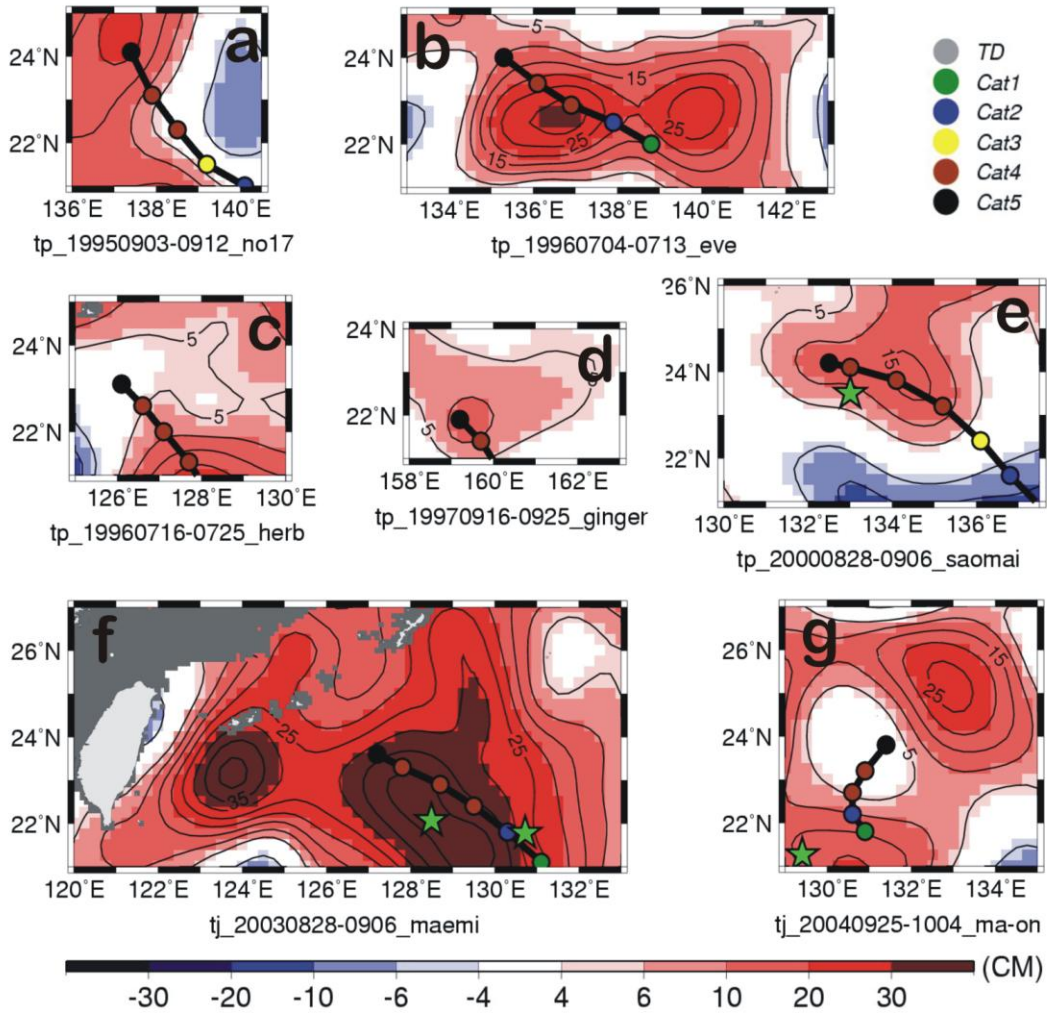
Fig. 12: Based on 13 years' (1993-2005) of observations, it is found that the warm ocean eddies in the South Eddy Zone of the Western North Pacific are important 'boosters' to restrain the self-induced cooling for typhoons to intensify to category-5 (From Lin *et al.* 2008)

The first mode showed an ENSO-like pattern, the second mode showed an El Niño pattern, and the third mode showed a central-Pacific warming pattern that looked like the Pacific Decadal Oscillation (PDO) pattern (Wada and Chan 2008). The third mode showed that an increase in the total number of TC's was accompanied with a warm central Pacific and cooler Northwestern Pacific Ocean. Negative TCHP anomalies in the Northwestern Pacific Ocean suggest that an increase in total number of TCs resulted in cooling due to their passages. On the other hand, the first mode showed that the number of super typhoons increased in mature El Niño years. An increase in accumulated TCHP upon first reaching the mature phase was related to the increase in the number of super typhoons due to their long duration.
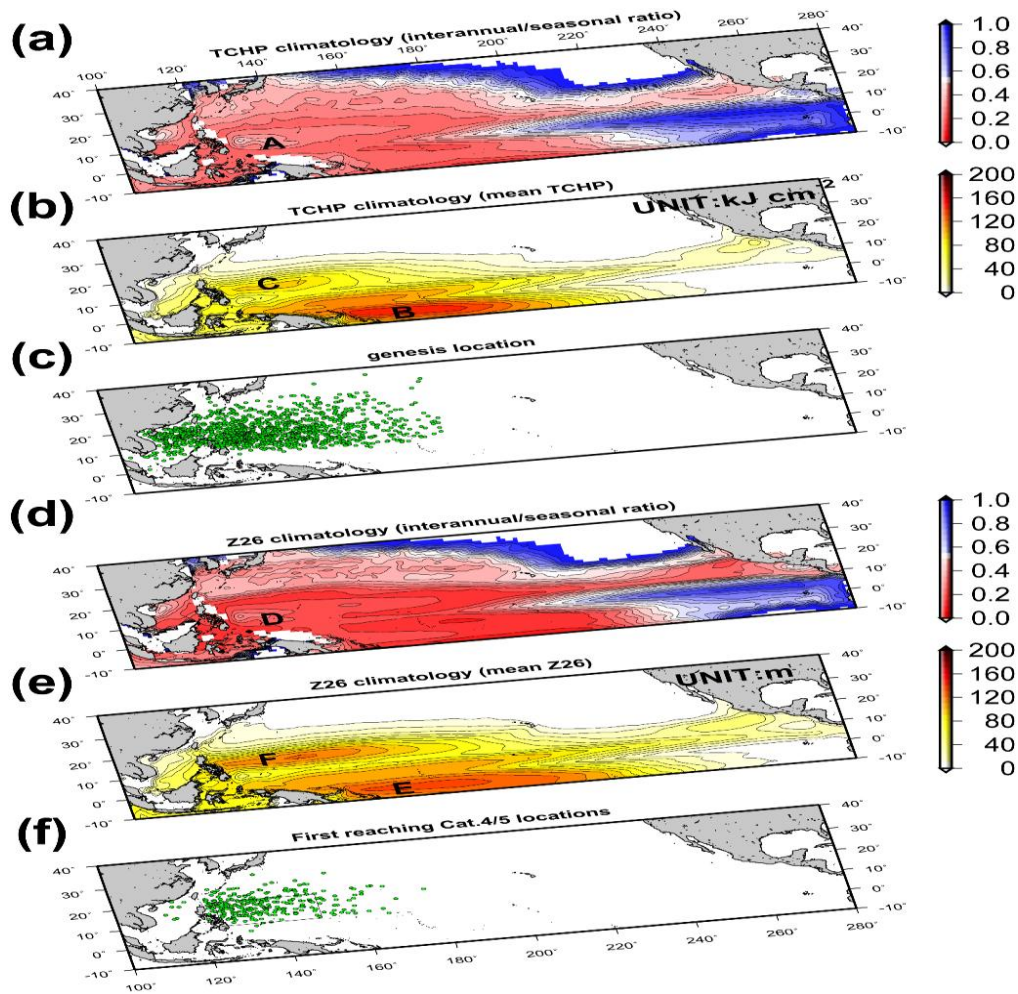
Fig. 13 Spatial distributions of (a) the ratio of root mean square of TCHP anomaly deviated from monthly mean TCHP for 44 years to that of the anomaly deviated from annual mean TCHP for 44 years, (b) TCHP averaged from 1961 to 2004, (c) genesis locations from JTWC best-track data, (d) as in Fig.1a except for Z26 and (e) as in Fig.1b except for Z26, (f) as in Fig. 1c except for the locations of TCs first reaching an intensity corresponding to cat-4 on the Saffir Simpson scale. Subscripts A-F shows high ratio of TCHP (A), high TCHPs (B, C), high ratio of Z26 (D) and high Z26s (E,F). (From Wada and Chan 2008).

In the Arabian Sea, beginning in May, a cyclonically rotating atmospheric vortex forms with similar characteristics to the TC in the Atlantic Ocean and the Gulf of Mexico basins (Rao 1984). This low-pressure center with cyclonically-rotating winds moves towards the northwest due to the migration of the InterTropical Convergence Zone (ITCZ) (Findlater 1969). The timing of this northward movement of the ITCZ is modulated by the Madden Julian Oscillation causing a few week lag in Southwest Monsoon onset. A low-level jet is formed (e.g., Findlater Jet) due to the convergence of the ITCZ and the persistent

18

northerlies over the northern portion of the Arabian Sea. In May 2003, Ali *et al.* (2007) found that this onset atmospheric vortex had characteristics similar to a TC (Fig. 14). The maximum intensity (Category-4 index) of the TC occurred over an oceanic regime where the SHA exceeded 20 cm (deeper OML) where the corresponding SST exceeded 30.5°C. The SHA field associated with this WCR is less compared to those in the GOM where SHA are 40 to 50 cm in surface deflection relative to mean sea surface level (Leben 2005).
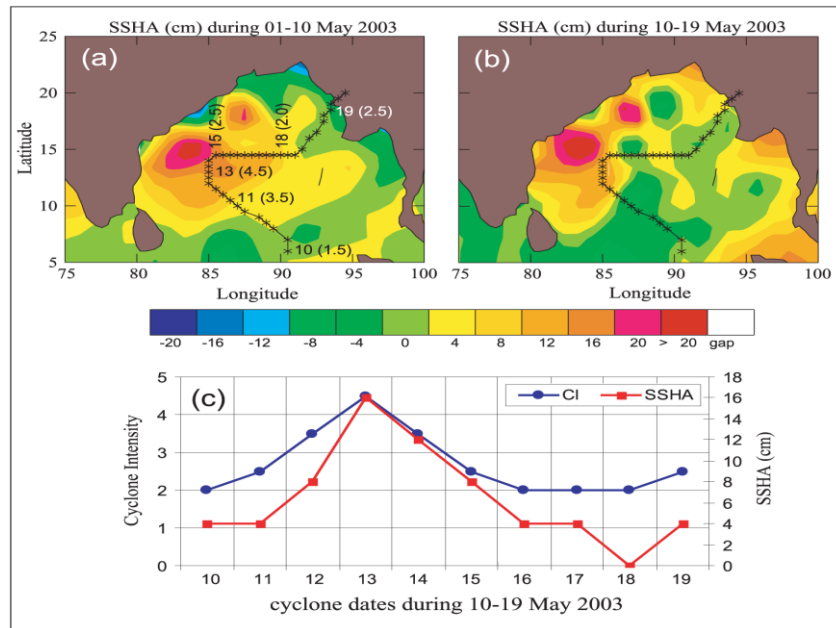

Fig. 14: Composite topography from several altimetry-derived sea-SHA field (SSHA: cm) from a) 1 - 10 May and b) 10-19 May 2003 relative to the TC track and c) the along-track time series variation of the SSHA and TC index (CI) for the Bay of Bengal cyclone (from Ali *et al.* 2007).

More recently, cyclone Nargis (2008) suddenly intensified from a relatively weak storm (category-1) to an intense category-4 storm within 24 hrs (Lin *et al.* 2009b). Based on a combination of satellite altimetry data, recently-available *in situ* Argo floats data, and numerical modelling, the abnormally thick sub-surface ocean warm layer (large OHC) precluded active entrainment of cooler, deeper thermocline water as found elsewhere. Thus, the ocean's negative feedback to cyclone's intensification is reduced and there is a substantial increase of the available air-sea sensible and latent heat fluxes to fuel Nargis' sudden intensification.

In the south Pacific Ocean, the Australian region experiences an average of 13 TC's per year and storms exhibit highly individual behaviours with erratic tracks (Dare and Davidson 2004). The ocean in this region is characterized by large environmental differences. Large mesoscale variability in upper OHC exists in various deep ocean areas, such as in the Timor Sea where activity is influenced by the Indonesian Throughflow and
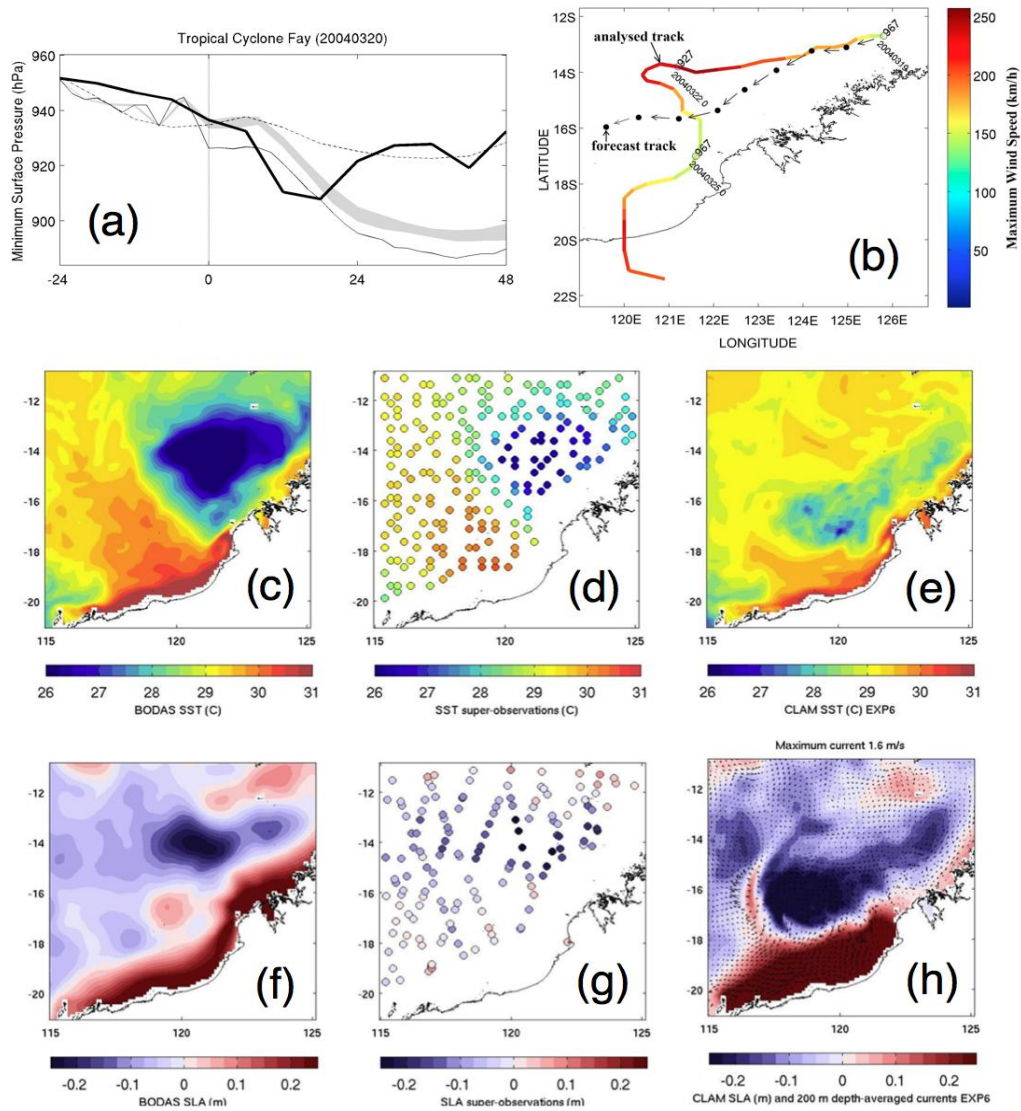
Fig. 15: Observation, analysis and prediction of the ocean response to tropical cyclone Fay at 24 March 2004 off the north-west shelf of Australia illustrating sensitivity of track forecast in coupled model. (a) Comparison of analysis (heavy solid-line), operational forecast (dashed-line), uncoupled CLAM forecast (thin solid-line) and ensemble of coupled forecasts (gray envelope) for minimum surface pressure. (b) Forecasted and analysed track. Post storm (c) BLUElink Ocean Data Assimilation system (BODAS) analysed SST. (d) SST super-observations from the AMSR-E microwave sensor and (e) simulated SST from CLAM. Figures f-h as per c-e and illustrate corresponding sea-level anomalies and depth-averaged currents up to maximum 200 m depth. (Adapted from Sandery *et al.* 2010).

the Coral Sea where variability is linked to the South Equatorial Current. Broad areas of shallow continental shelf seas also exist, such as the Gulf of Carpentaria and the North West Shelf where relatively isothermal conditions prevail. The coexistence of different oceanographic environments and the broad extent of the shelf break often leads to the presence of fronts with sharply varying OHC.

Furthermore, a relatively higher degree of stratification is found in the equatorial south-west Pacific compared to the Atlantic, which means that a larger amount of work may be required to break down the potential energy and mix cooler water to the surface. Most TCs encounter the mixture of oceanographic regimes at various stages of their lifetime, meaning that that the oceans role is complex, varied and specific for each case. There are a significant number of cases where observations show large degrees of induced SST cooling that have led to a significant change in storm intensity. One such case is TC Fay that occurred off the north-west shelf region in March 2004. This case is an example that illustrates the sensitivity of the ocean response and TC intensity to forecasted track (Sandery *et al* 2010). Here, the forecasted track led to the storm centre following the shelf break where no cooler subsurface water was available on the left side of the storm. The actual track veered ~50 km off the shelf break over significantly deeper waters and the storm produced a pronounced ocean cooling response that significantly modified the storms intensity (Fig. 15). This illustrates that a skilful coupled model will be required to correctly estimate intensity change for TCs in the Australian region.

Similarly, Katrina and Rita as they both deepened to a Cat-5 TC over a lobe-like structure along the LC's western flank (Scharroo *et al.* 2005; Shay 2009; Jaimes and Shay 2009). There was a one-to-one correlation between TC intensity (surface pressure decreases) and OHC values exceeding 100 kJ cm^{-2} in the LC. By contrast, SSTs of more than 30°C were nearly uniformly distributed in this regime, and did not reveal the complex LC and WCR structure in the central Gulf of Mexico (Sun *et al.* 2006; Shay 2009). This OHC level is more than five times the threshold of 17 kJ cm^{-2} d^{-1} integrated over the TC scale (Leipper and Volgenau 1972). Normalized OHC values vary inversely to pressure changes (surface pressure decreases, OHC increases). Mainelli *et al.* (2008) input OHC into the SHIPS (DeMaria *et al.* 2005) and found that OHC is a better indicator of TC strength than just SST alone which is similar to when TC Opal (1995) encountered a WCR and deepened to a category-4 TC during favorable atmospheric conditions. Clearly, In the WPAC, Indian Ocean and GOM ocean basins, these cases are all examples of *less negative feedback* since the upper ocean cooled by less 2°C to ~28°C in regimes of deep warm layers (e.g., not much of a cold wake). Thus, the depth of the 26°C isotherm, usually located close to the depth of the OML, and the resultant OHC is relevant to TC intensity changes.

1.3.3.4 Evaluation of OHC

Given the availability of the satellite-derived values of OHC derived from radar altimetry over the globe, it is imperative to assess these inferred values relative to *in situ* data profiles (Pun *et al*. 2007; Jaimes and Shay 2009; Shay and Brewster 2010). To illustrate
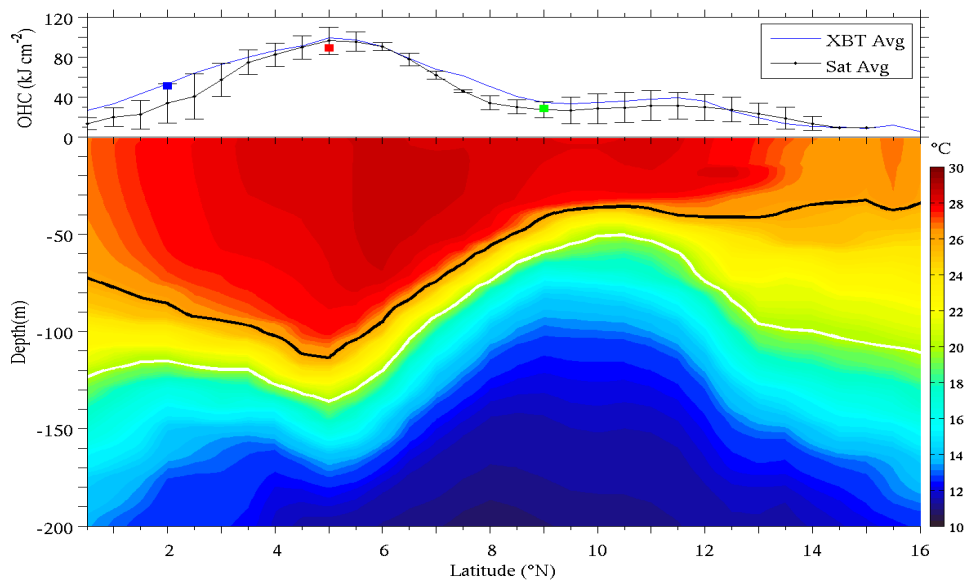
Fig. 16: Average OHC (upper panel: kJ cm^{-2}) from repeat XBT transects in the eastern Pacific Ocean basin (blue line), TAO moorings at 2, 5 and 8°N (140°W: colored boxes) and the corresponding satellite-derived values (black line) with $\pm 2\sigma$ and the corresponding vertical temperature structure from the XBTs (lower panel) where the depth of the 20°C isotherm (white line) and the 26°C (black line). Data are averaged from the months of July from 2000 to 2005 (From Shay and Brewster 2010).

the validity of this OHC approach from altimetry under non-forcing conditions, satellite-derived values were compared to *in situ* measurements from XBT transects in the eastern Pacific Ocean basin (Shay and Brewster 2010). Five years of data along a repeated transect is used to determine OHC and compare it to the five-year average from satellite-inferred values along the same transect as well as the closest moorings (Fig. 16). There is marked agreement between the XBT, mooring and satellite-derived OHC values. Notice there are no significant differences between the two *in situ* and the remotely sensed values at 95% confidence. Over a broader spatial scale from 2000 to 2008 during the EPAC basin hurricane season, OHC value statistics from 6,420 *in-situ* data points revealed RMS OHC differences were 13 to 20 kJ cm^{-2} or up to 15% of the maximum values with an RMS difference of 17 kJ cm^{-2} (not shown). Thus, estimating the 26°C isotherm depth using satellite altimetry in a reduced gravity model (Goni *et al.* 1996) allows one to determine OHC for use with SHIPS (DeMaria *et. al.* 2005; Mainelli *et al.* 2008) that must be applied globally.

An updated oceanographic climatology has been developed for the developed empirical calculating OHC known as Systematically Merged Atlantic Regional Temperature and Salinity (SMARTS) Climatology. SMARTS was developed by regionally blending the World Ocean Atlas 2001 (WOA) and Generalized Digital Environmental Model v.3.0

22

(GDEM) monthly climatologies at 1/4º resolution. This higher resolution climatology better resolved the spatial structure of the LC and eddy features in the GOM, improving upon Mainelli *et al.* (2008) approach.
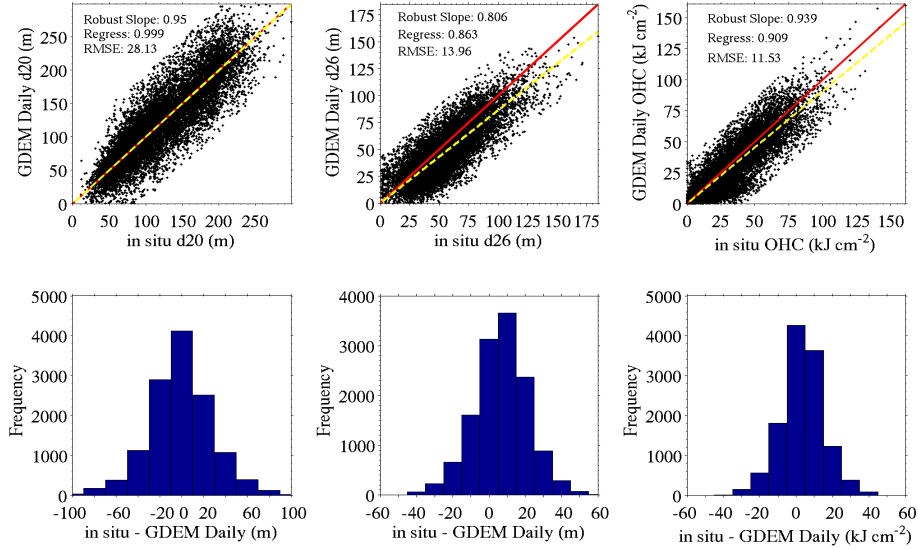

Fig. 17: Scatter plots (upper panels) of is situ versus satellite derived d_{20} (m), d_{26} (m) and OHC (kJ cm^{-2}) and frequency distribution of in situ–satellite inferred differences (lower panels) from temperature profiles sensed by ARGO floats in the Atlantic Ocean basin using SMARTS and altimetry. In the scatter plot, the red line is the slope of the perfect fit, the yellow-dashed line is the slope of the actual regression fit. Key statistics are located in the upper left side of the scatter plots (From Meyers *et al.* 2010).

Using SSTs from TMI AMSRe measurements for the surface boundary conditions, satellite-derived OHC, D_{20}, and D_{26} were calculated daily from 1998 to present using WOA and GDEM. To determine the skill of WOA and GDEM, satellite estimates were compared to over 44,000 in-situ profiles from shipborne and airborne XBTs, long-term PIRATA moorings, and Argo drifters. As shown in Fig. 17 a direct relationship has emerged from the detailed analysis between satellite-derived and *in-situ* measurements of isotherm depths and OHC. The climatology was specifically examined in the GOM, LC, Gulf Stream, and equatorial wave guide to statistically calculate spatial blending weights from WOA and GDEM for the daily high resolution product (Meyers *et al.* 2010).

1.4 Air-Sea Interface:

The effect of the underlying ocean has drawn attention towards gaining a better understanding of the physical interaction between the atmosphere and ocean during TC's. Due to limited observations across the air-sea interface in high-wind conditions, the understanding has not progressed nearly enough to significantly improve the parameterization of momentum and energy transfers between the two fluids. The

23

relationships of the transfer processes of small-scale roughness (Charnock 1955) and surface-layer stability (Monin-Obukhov similarity theory) are understood under low- to moderate-wind conditions (Large and Pond 1981), but additional phenomena not typically observed such as the sea state maturity (Donelan 1990; Moon *et al.* 2004a,b) and sea spray (Wang *et al.* 2001; Andreas 2010) have been shown to modulate the heat and momentum exchange. These effects under TC winds have been primarily studied in controlled laboratory experiments (Donelan *et al.* 2004). In a TC environment, both young and mature waves are present and impact air-sea fluxes and OML and atmospheric boundary layer processes.

Intensity is maintained in part by the balance between the heat gained by the atmospheric boundary layer and the energy lost due to friction. Emanuel (l986) proposed a theory requiring this relative balance to be a primary modulator of maximum potential intensity (MPI). Based on this view, it is assumed that under certain conditions there should be a level of mutual dependence of the air-sea transfer processes of heat and momentum as suggested in idealized model simulations (Emanuel 1995; Braun and Tao 2000). This has led to the conclusion that intensity is sensitive to the ratio of enthalpy to drag coefficient ($c_k c_d^{-1}$), which lies within a limited range. However, most TCs do not reach their MPI (DeMaria *et al*. 2005).

1.3.4.1 Surface Wave Field

In 1993, TC Emily approached NOAA buoy 44014 from the southeast with sustained winds of 28 m s^{-1}, the significant wave heights reached 8 m (Fig.18) where maximum wave spectral energies were contained in the swell portion of the spectrum (i.e., ~13 s wave) that decayed rapidly after TC Emily's passage. These wave spectral energies contained in the lower-frequency intervals associated with the swell began several hours in advance of storm passage, peaking at the point of closest approach, and decayed over 1 to 2 IPs. In the wake of a TC, the barotropic trough in the surface height field contains IP fluctuations of 4 to 7 cm due to the vertically integrated mean mass divergence field (Shay and Chang 1997). By contrast, in baroclinic models (e.g., rigid lid), these IP oscillations do not exist as the vertical velocity is zero at the free surface as per the kinematical boundary condition. In frequency bands between 0.2-0.4 Hz, IP undulations in the surface height affect wave spectral energies for an extended period of time (Faber *et al.* 1997) as suggested by the peaks in both wave spectral energies and significant wave heights. More recently, TC Lili approached buoy 42001 from a south-southwest direction just after reaching maximum intensity (Cat- 4). As Lili passed within ~ Rmax to the west of the buoy, winds reached 48 m s^{-1}, significant wave heights peaked above 10 m, and wave spectral energies exceeded 220 m^2 Hz^{-1} (Fig. 18b). This is the region of the storm where the maximum ocean response is often observed as noted above. The largest values of wave spectral energy were concentrated in the lower frequency band with maximum values at 0.4 IP (~10 h) prior to passage and persist for about 1.5 IP (~40 h) after the closest approach of Lili. Smaller amplitudes of the wave spectral energy in the higher frequency (0.2-0.4 Hz) intervals are evident 1.7 IP (~48 h) prior to passage, and persist after Lili's

passage over the buoy. The phase of these oscillations, which is most pronounced between the frequency intervals 0.2-0.4 Hz, is near the local IP (~27 h).
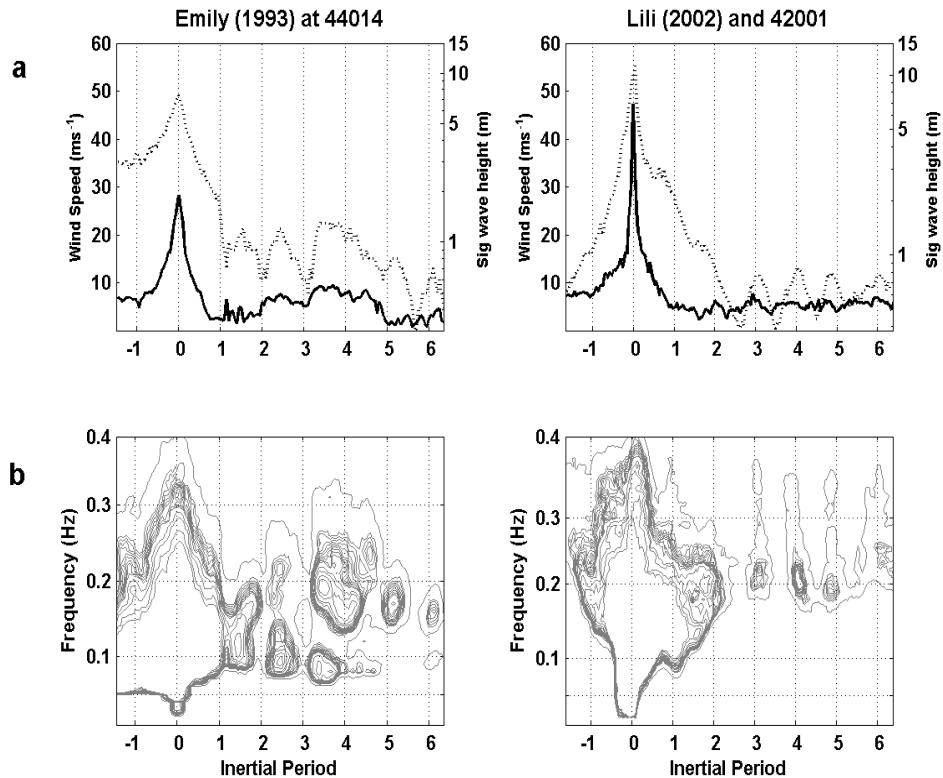

Fig. 18: Time series of a) wind speed (solid) and significant wave height (dotted), and b) wave spectral energy (0.1 to 1 m^2 Hz^{-1}) from buoys 44014 and 42001 during and after Emily (left) and Lili (right). Time is scaled by local IP ~20 hrs for NOAA buoys 44014 and ~27 hrs for 42001.

Wang *et al.* (2005) documented the wave response to Ivan over the NRL SEED moorings (Fig. 19). Wave heights increased with peak values when the radial distance between the mooring and storm center was ~75 km (Fig. 19 c). Hs reached maximum values of 16 m to 18 m on inshore moorings and were larger than those detected at the NDBC buoy (15.9 m). The maximum wave height was recorded to be 27.7 m at mooring 3, and wave height variations were consistent with the radial variations in the surface wind of Ivan. At Rmax, the model predicted a maximum wave height of ~21 m. Previous studies have suggested in a TC wave field that the maximum wave height approaches 1.9 x Hs, which would be consistent with these measurements. However, the moored measurements sampled only a small part of the domain influenced by Ivan's broad wind field with large changes in the bottom topography.
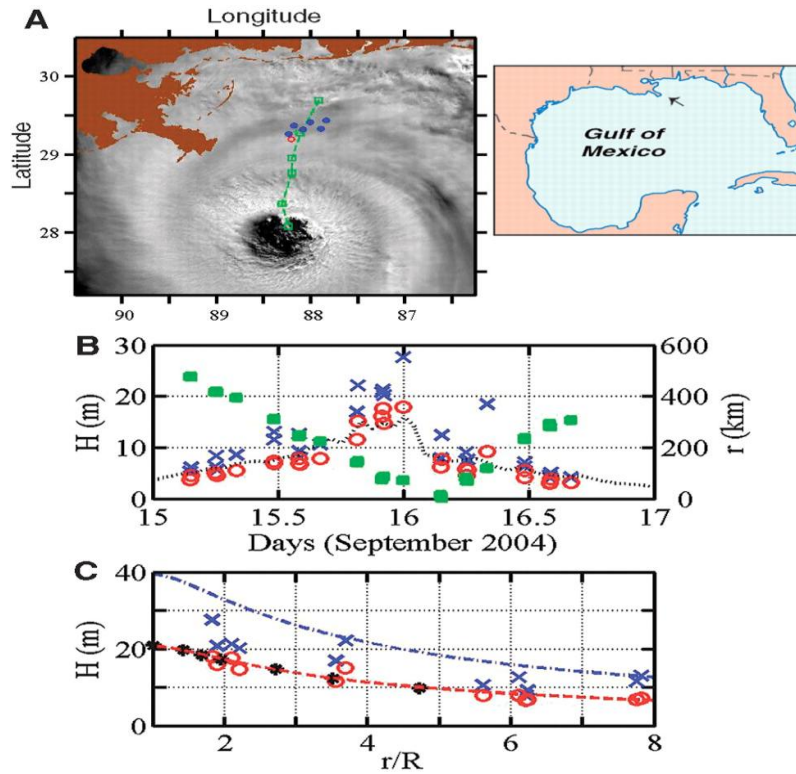
Fig. 19: a) TC Ivan image at 1850 UTC 15 Sept 2004 with the green line representing the track of Ivan at 3-h intervals moving over the SEED moorings (blue). Panel b) represents the time evolution of Hs (circle) and Hmax (cross) at differing distances. Hs is from NDBC buoy 42040 (dotted curve) and its radial distance to Ivan's center is shown by the green squares. Panel c) represents Hs and Hmax as a function of normalized distance from the center compared to the exponential distance: digitized values of a segment 15° CW from the forward direction of a numerically simulated wave field (black asterisks). Blue curve depicts the line of Hmax = 1.9Hs where circles and crosses are as in panel b) (from Wang *et al.* 2005).

1.3.4.2 Surface Winds

Surface winds in hurricanes have been estimated remotely using the Stepped-Frequency Microwave Radiometer (SFMR) from aircraft (Uhlhorn *et al.* 2007). With six frequencies, the SFMR measures radiative emissions, expressed in terms of brightness temperatures (T_b), from the ocean and the atmosphere. The percentage of foam coverage on the sea surface is known to increase monotonically with wind speed. At microwave frequencies, foam acts as a blackbody emitter. As foam increases, the ocean emits microwave energy more readily, and assuming a constant SST, the T_b increases. Given an accurate physical model that relates ocean surface wind speed and rain-rate to measurements of T_b at each frequency, a set of equations are inverted to estimate surface winds. Based on measurements during the 2005 Atlantic hurricane season, Uhlhorn *et al.* (2007) developed
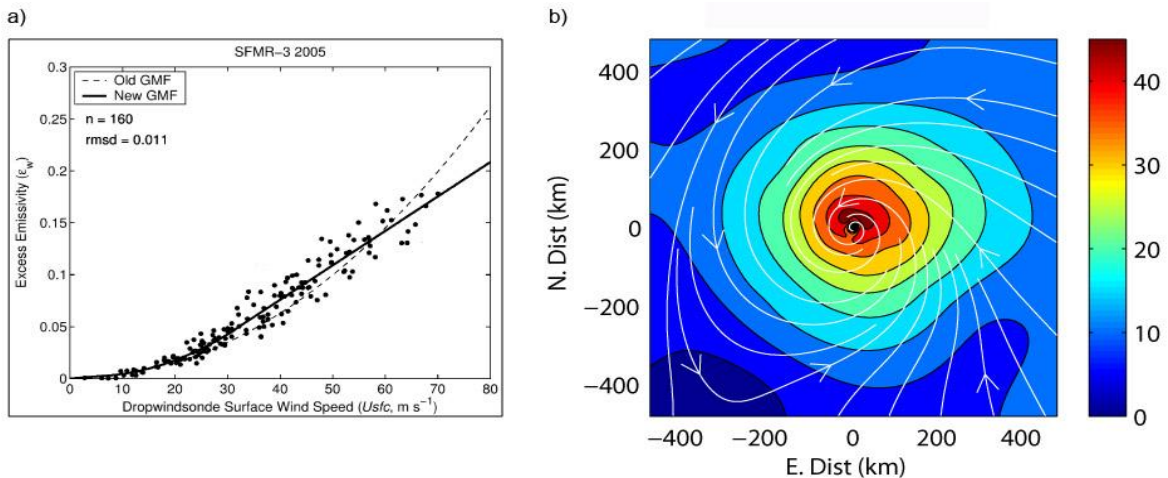
Fig. 20: a) Excess emissivity from SFMR compared to 10-m surface winds measured from GPS dropsondes. The total number of samples is 160 and the RMS difference between the SFMR model function was 0.011 (left panel) and b) example of an HWIND wind field (Powell and Houston 1996) and streamlines relative to the TC center (0,0) when SFMR data are included into the analysis from TC Frances (2004) where the color bar is in m s^{-1} (from Uhlhorn *et al.* 2007).

a new emissivity and wind speed model function based on comparisons with direct measurements of surface winds in hurricanes by GPS dropwindsondes (Fig. 20). This function eliminates a previously-documented high bias in moderate SFMR-measured wind speeds (10 to 50 m s^{-1}), and additionally corrects an extreme wind speed (>60 m s^{-1}) systematic underestimate in the past cases. The model function behaves differently below and above the hurricane wind speed threshold (32 m s^{-1}), which may have implications for air-sea momentum and kinetic energy exchange.

1.3.4.3 Surface Drag Coefficient

Knowledge of the heat and moisture fluxes across the interface and into the atmospheric boundary layer are critical elements (Emanuel 1995). Momentum transfer between the two fluids is characterized by the variations of wind with height and a c_d that is a function of wind speed and surface roughness. For more than a decade, GPS sondes (Hock and Franklin 1999) have been deployed from aircraft to measure Lagrangian wind profiles in the TC boundary layer. By analyzing these profiles, Powell *et al.* (2003) found a logarithmic variation of mean wind speed in the lowest 200 m, a maximum speed at 500 m, and a gradual weakening with height to 3 km. From these estimates, the surface stress, roughness length, and neutral stability drag coefficient determined by the profile method suggest a leveling of the surface momentum flux as winds increase above hurricane-force and a slight decrease of the drag coefficient with increasing winds.
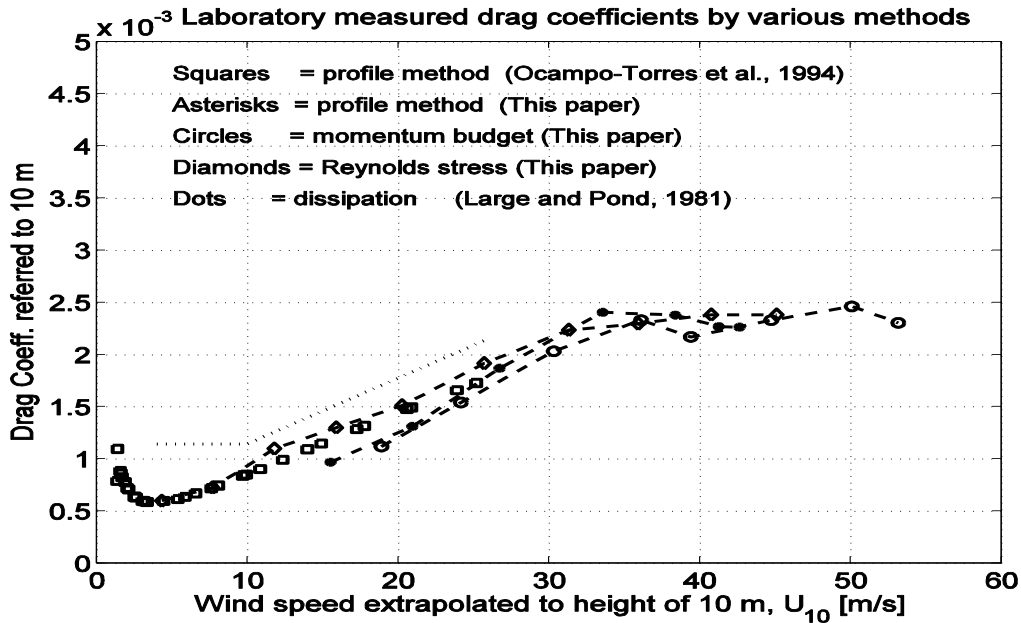
Fig. 21: Laboratory measurements of the neutral stability drag coefficient (x 10^{-3}) by profile, eddy correlation ("Reynolds"), and momentum budget methods. The drag coefficient refers to the wind speed measured at the standard anemometer height of 10 m. The drag coefficient formula of Large and Pond (1981) is also shown along with values from Ocampo-Torres *et al.* (1994) derived from field measurements (from Donelan *et al.* 2004)

Donelan *et al.* (2004) described a series of wind-wave tank experiments that included stress measurements from hot-film anemometry and digital particle image velocimetry, and laser/line scan cameras for measuring the water surface elevation. Measurements of the drag coefficient from this laboratory experiment, referenced to the 10-m wind speed, are shown in Fig. 21. Wind speed was measured at 30 cm height in the tank and extrapolated to the 10-m using the logarithmic dependence on height. Wind speeds were verified between crest height and 30 cm for all but the two highest wind speeds. Wind changes both direction and speed over relatively short distances in a TC compared to those required to approach full wave development. The largest waves in the wind-sea move slowly compared to the wind and often travel in directions differing from the wind. Under such circumstances, these long waves contribute to the aerodynamic roughness of the sea as hypothesized by Kitaigorodskii (1968) and demonstrated by Donelan (1990). Measurements at sea (e.g., Large and Pond, 1981) and in laboratories demonstrate the increasing aerodynamic roughness with increasing wind speed. A "saturation" of the drag coefficient does appear once the wind speed exceeds 33 m s^{-1} (Fig. 21). Beyond this speed, the surface does not become any rougher. At the highest wind speed, significant height and peak wave frequency in the laboratory were 9 cm and 1.4 Hz, respectively.

From 10 to 26 m s^{-1} wind speeds, these measurements parallel the ocean measurements (Large and Pond 1981), but are less energetic.

The saturation level for c_d is ~0.0025, corresponding to a roughness length of 3.35 mm from the laboratory results. Powell *et al.* (2003) found a "saturation" of the drag coefficient at 0.0026 at about 35 m s^{-1} that decreased at higher wind speeds using wind profiles normalized by a mean boundary layer wind. Shay and Jacob (2006) found a "saturation" wind speed at 30 m s^{-1} of 0.0034 derived by equating internal wave ocean fluxes to the surface winds at 10-m level. Note it was assumed that all of the wind drives a current and no separation was attempted here to partition the energy between current and wave fields. Beyond 30 m s^{-1}, the c_d began to leveled off at surface wind speeds up to 38 m s^{-1} observed in TC Gilbert. The implication here is that ocean current profilers deployed in TC can be used to trace the momentum flux, and the c_d behavior.

The momentum flux was also estimated using the current profiles recorded in water depths of less than 100 m during TC Ivan (Teague *et al.* 2007), and discussed in terms of the neutral drag coefficient (Jarosz *et al.* 2007). The eye of Ivan generated a strongly forced and relaxation stage responses to the surface wind field (Wang *et al.* 2005; Teague *et al.* 2006, 2007). Over the shelf, the response consisted of a barotropic component , and a much weaker baroclinic response. Scale analysis of recorded current velocity showed that this forced response was described by the linearized, depth-integrated along-shelf horizontal momentum balance with bottom friction. The drag coefficient was estimated based on these observed depth-averaged currents at an ADCP mooring for wind speeds between 20 and 48 m s^{-1}. In this case, surface drag increased to a peak value of 0.0026 at 32 m s^{-1} before decreasing. This inflection point is coincident with above results. Differences may also be attributed to uncertainties in the wind measurements and the use of simplified ocean dynamics.

Recently, Sanford *et al.* (2007) estimated the volume transport per unit of width based on velocity profiles in hurricane Frances using a saturated surface drag coefficient of Powell *et al.* (2003) and L:arge and Pond (1981) formulations. Numerical simulations from the PWP mixing model embedded in the 3-Dl ocean model (Price *et al.* 1994) indicated consistent results for the volume transport and SST cooling values at two of the three floats to the right of the storm track. Along the track, however, differences differed by about 15 to 20%. As Sanford *et al.* (2007) point out, perhaps an azimuthal dependence in the surface drag coefficient due to surface waves (Wright *et al.* 2001) must be included in the models as well as wind-field asymmetries common to most TCs. In this context, additional case studies must be performed to understand how the waves, winds and currents are coupled under high-wind conditions (Bender and Ginis 2000; Bao *et al.* 2000; Rogers *et al.* 2006; Drennan and Shay 2006; Black *et al.* 2007; Chen *et al.* 2007)
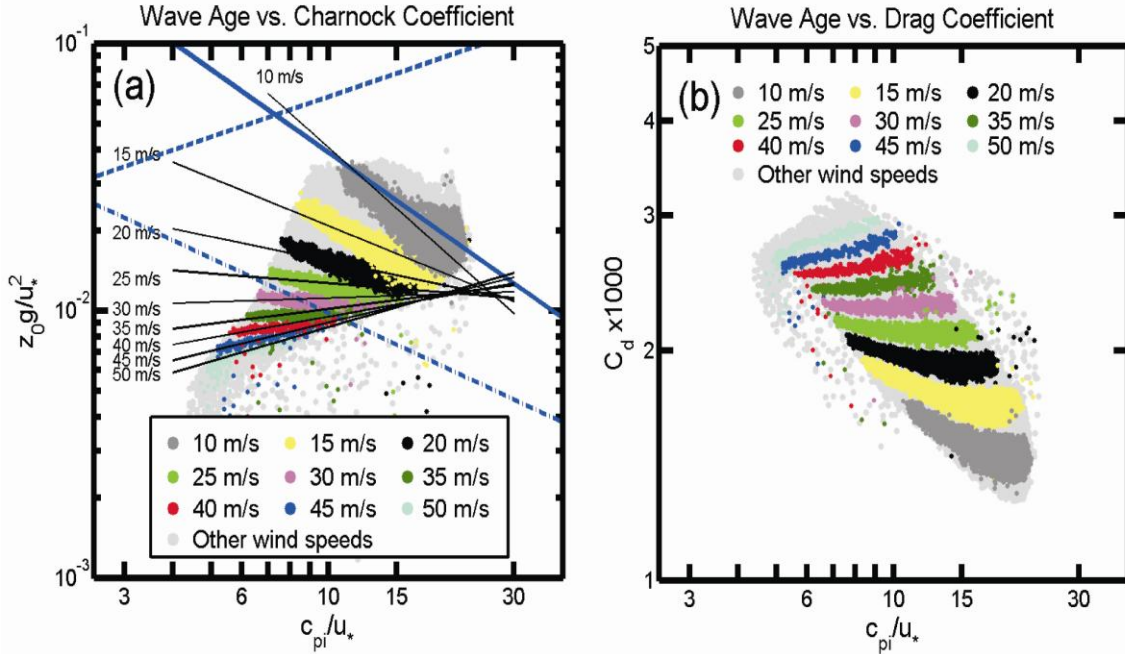
1.3.4.4 Wind-Wave Coupling

Fig. 22: Scatterplots of the a) Charnok Coefficient (z_{ch}) and b) drag coefficients (c_d) as a function of the wave age (cp/ u∗) for several TCs in the Atlantic Ocean. Differing colors represent 5-m s^{-1} intervals for surface winds for z_{ch} and c_d are the best fits for each wind speed group. In panel a, blue solid line and dash-dot represent empirical estimates for ocean and laboratory experiments (Donlan 1990). Dotted line is the formula of Toba et al. (1990) (Figure from Moon *et al.* 2004a).

The momentum flux is parameterized with a non-dimensional surface roughness (or Charnock's equation, $z_{ch} = z_0 g / u_*^2$, where z_0 is the roughness length, u_* is the surface friction velocity and *g* is the gravitational acceleration) and the stability correction (not shown) is based on the Monin-Obukhov similarity theory, regardless of the wind speed or the sea state in the GFDL model. Moon *et al.* (2004) investigated the Charnock coefficient under TC conditions using a coupled wind-wave (CWW) model (Fig. 22). In the CWW model, the surface wave directional frequency spectrum near the spectral peak is calculated using the WAVEWATCH III (Tolman 2002) model and the high frequency part of the spectrum was parameterized using the theoretical model of Hara and Belcher (2002). The wave spectrum is then introduced to the wave boundary layer model of Hara and Belcher (2004) to estimate the Charnock coefficient at differing wave evolution stages. The regression lines between the wave age and the Charnock coefficient have a negative slope at low wind speeds but have a positive slope at higher wind speeds. For example, in Figure 22a, this change in slope occurs between 25 and 35 m s^{-1}. This behavior of the Charnock coefficient provides one explanation why c_d under a TC, where seas tend to be "young," is reduced in high wind speeds as the wave field is not fully developed.
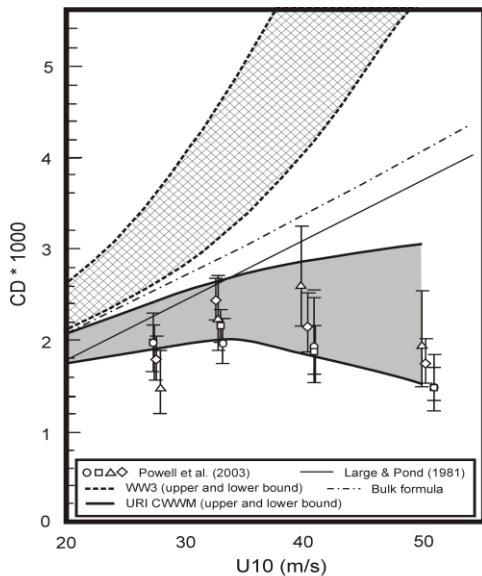
Fig. 23: Drag coefficients (C_d) from various observation-based values, empirical formulas, and model outputs as a function of U_{10}. Symbols represent observations from GPS sonde wind profiles (Powell et al. 2003). Vertical bars represent 95% confidence limits. Solid line is an extrapolation of the Large and Pond (1981) formula. Dash-dot line is the bulk formula used in GFDL hurricane model. Shaded and hatched areas represent ranges between upper and lower bound of C_d obtained by the URI coupled wave-wind model and an internal estimation of WAVEWATCH III, respectively (from Moon et al. 2004).

Consistent with this change in the Charnock coefficient, c_d levels off at high wind speeds and begins to decrease at ~35 m s^{-1} (Fig. 23). The result also is in accord with these other studies in that the drag coefficient levels off between surface winds of 28 to 33 m s^{-1} and begins to decrease with wind speeds (Powell *et al.* 2003; Donelan *et al.* 2004). Notwithstanding, perhaps the most important finding of the Moon *et al.* (2004b) study is that a hurricane model must have a surface wave model to gain a more accurate prediction of surface enthalpy fluxes under the high-wind conditions.

Another potentially important limiting factor in TC intensification is the kinetic energy loss due to surface friction. The viscous dissipation of the kinetic energy can be a significant heat source for TCs as this part of the kinetic energy is ultimately dissipated on molecular scales into heat (Bister and Emanuel 1998). Using the Navy's operational forecast model - Coupled Ocean/Atmosphere Mesoscale Prediction System (COAMPS®) to improve TC intensity and structure forecasts, Jin *et al.* (2007) showed that the inclusion of dissipative heating improves surface maximum wind forecasts of Hurricane Isabel by 10-20% at a 15-km horizontal resolution and even more so (up to 29%) at 5-km resolution. This study is distinct from previous investigations of dissipative heating (e.g. Zhang and Altshuler 1999) in that the kinetic energy dissipation both at the surface and in the internal atmosphere is considered using the dissipation equation of turbulent kinetic energy (TKE) to ensure energy conservation. The averaged profiles of the wind speed in the boundary layer indicate that the TKE-only run (only the dissipative heating in the internal atmosphere considered) results in a small impact on wind speed, but when the dissipative heating from the surface friction and internal dissipation work together the storm obtained significantly stronger winds than when either process at work alone (surface friction only or TKE only), suggesting highly nonlinear interaction between the two dissipative heating

---

COAMPS® is a registered trademark of the Naval Research Laboratory.

processes. The dissipative heating produced about 12 m s^{-1} stronger azimuthally averaged winds in the eyewall region than the run without and also warmed the air near the surface by nearly 1°K near the eyewall, resulting in negative (albeit small) sensible heat flux in that region. The azimuthally averaged vertical motion in the run without the dissipative heating was only about 0.5 m s^{-1} over a section of 60 km along the radius.
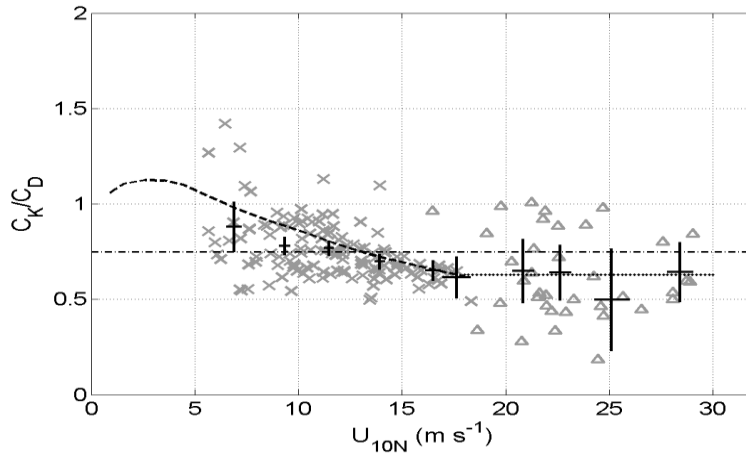
1.3.4.5 Enthalpy Fluxes

Fig. 24: The ratio of c_k/c_d as a function of 10-m neutral wind speed. Data from CBLAST (Δ), and HEXOS (x) are shown. Solid black lines show the mean and 95% confidence intervals of the combined HEXOS and CBLAST field data after binning average by wind speed. The dotted black line shows the mean of the CBLAST data. The ratio based on COARE 3.0 bulk flux algorithm is shown as the dashed line. The threshold value of 0.75 suggested by Emanuel is also shown as the dash-dotted line (from Zhang 2007).

Direct turbulent flux measurements were carried out in the hurricane boundary layers using a research aircraft instrumented with fast-response turbulence sensors (Black *et al*. 2007). As shown in Fig. 24, the wind speed range for momentum and enthalpy fluxes and exchange coefficients has been extended by over 50% compared to that in previous studies. The drag coefficient (c_d) increase linearly with 10 m wind speed up to 22 m s^{-1} then level off at higher wind speed (French *et al*. 2007). The Dalton number (c_E) is nearly constant with 10 m wind speed up to 30 m s^{-1} (Drennan *et al*. 2007). Combining the sensible and latent heat flux measurements, Zhang (2007) derived the enthalpy flux and the exchange coefficient for enthalpy transfer (c_k) showing that there is no evidence of an increase of c_k with wind speed, in good agreement with the Humidity Exchange over the Sea (HEXOS) result (DeCosmo *et al*. 1996) . The ratio of c_k/c_d versus wind speed for the flux runs with both momentum and enthalpy flux measurements. The average of the c_k/c_d values is 0.63 well below the 0.75 threshold for TC development suggested by Emanuel (1995).

Estimates of enthalpy fluxes during TC's Isidore and Lili were sensitive to the storm translation speed. In Isidore, peak enthalpy flux ~1.7 kW m^{-2} is in the right-rear quadrant of the storm due to the high SSTs (~30°C) as there was a negligible decrease from pre-storm SST conditions, especially over the warm LC where ocean cooling was minimal (Shay and Uhlhorn 2008). Although the maximum momentum flux (7 Pa) is in the right-front quadrant, TC Isidore's wind stress field was symmetric as it moved at only 4 m s^{-1}. Estimated maximum surface enthalpy fluxes in Lili were about 1.4 kW m^{-2} due in part to the marked asymmetry associated with the faster storm translation speed (7 m s^{-1}) and smaller SSTs by about 1°C. This result highlights how modest SST differences alter the surface heat fluxes in extreme winds (Cione and Uhlhorn 2003). Enthalpy fluxes were integrated along the track to obtain the cross-track (radial) distributions of net sea surface heat loss (not shown). The estimated surface heat loss in Isidore (~9 kJ cm^{-2}) is almost a factor of two larger than in Lili (~4.5 kJ cm^{-2}) due to the enhanced enthalpy fluxes, slower storm speed, and larger horizontal SST gradients along the western side of the Yucatan Strait.

Observations obtained from an automatic measuring system for the partial pressure, pCO_2, of atmospheric and oceanic carbon dioxide clearly showed rapid variations in oceanic pCO_2 during the passage of three typhoons in 1997 (Nemoto *et al.* 2009). The effects of typhoons on surface ocean-atmosphere CO_2 exchange could differ depending on the relative position to the mooring site with respect to the center position of the moving typhoons. The difference arose from a difference in the contributions of entrainment and upwelling to rapid decreases in sea-surface temperature. The estimated efflux enhanced by typhoons Tina, Winnie and Oliwa (1997) accounted for 60% of CO_2 efflux.

1.3.4.6 Sea Spray

Recent research on sea spray effects in TCs has included fundamental theory, surface-source scaling, near-surface effects of spray on momentum and thermodynamic transfer, and sensitivity of numerical forecast models to parameterized sea spray. Soloveiv and Lukas (2010) postulated a lower limit on the drag coefficient under hurricane force winds caused by the break-up of the air–sea interface due to Kelvin–Helmholtz instability and formation of the two-phase transition layer consisting of sea spray and air bubbles. Rastigejev and Lin (2010) applied the Lighthill and Barenblatt approach to examine the lubricating effect of sea spray associated with it negative buoyancy effect.

Several new scaling models for the spray source strength (Kudrayetsev and Makin, 2009; Mueller and Veron, 2009; Fairall *et al.* 2009) were published where the source strength was linked to wave and breaking wave properties. The Fairall *et al.* (2009) work included laboratory verification of some of the model assumptions. Vickery et al.'s 2009 analysis of wind profiles from low-level dropsondes found that the drag coefficient, given similar wind speeds, is smaller for smaller-radii storms; enhanced sea spray by short or breaking waves was speculated as a cause Andreas (2010) published a scaling parameterization of the heat and salinity fluxes at high winds. Several papers (Kihara and Hirakuchi 2008;

Innocentini and Goncalves, 2010; Bianco *et al.* 2010) have appeared that essentially use very high-resolution 1-D models to study the effects of injection, acceleration, and evaporation of sea spray on near-surface profiles of winds, temperature, humidity, and their fluxes.
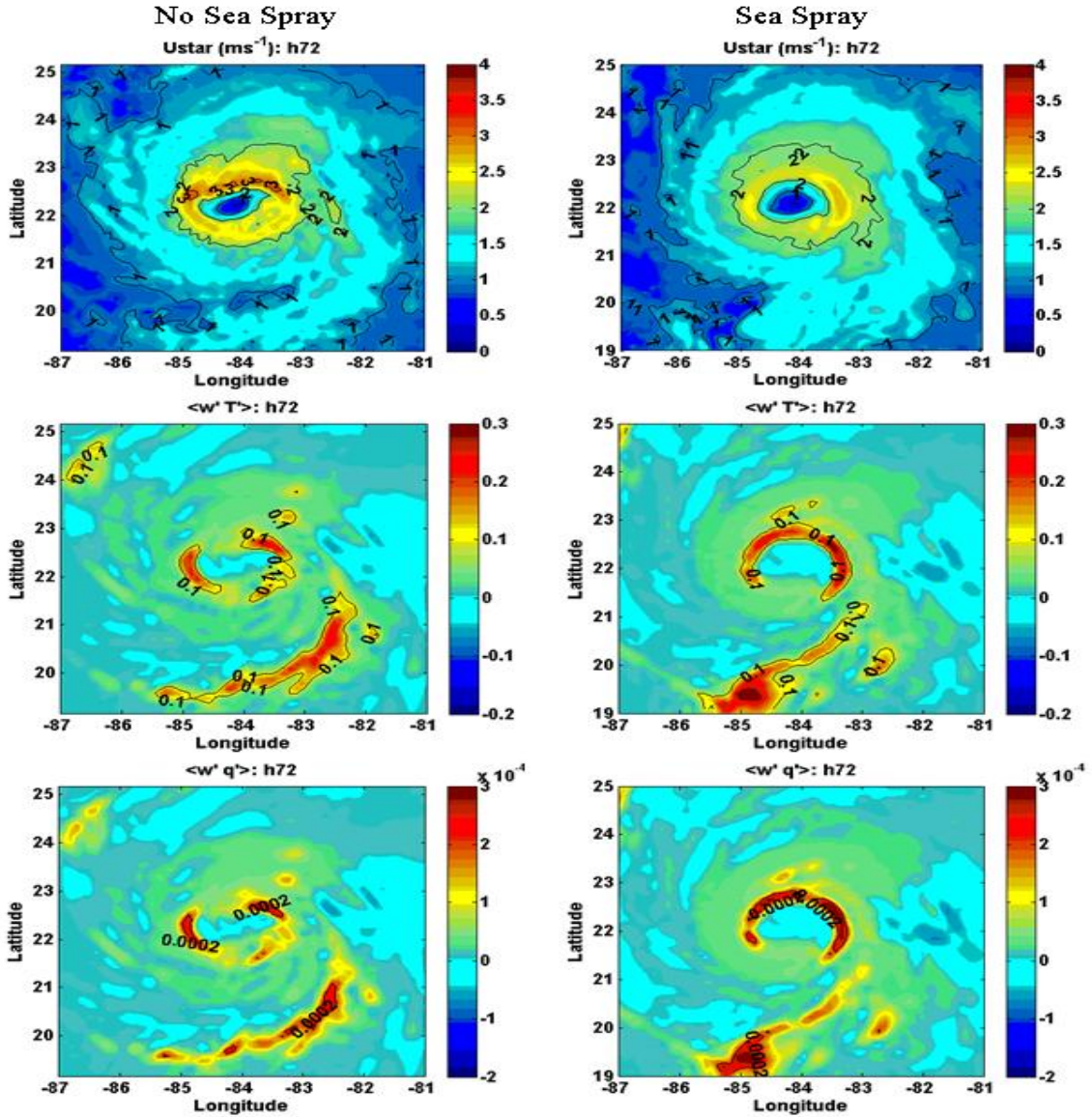

Fig 25: Maps of the friction velocity (u*, the top row, in unit of ms^{-1}), turbulent flux of temperature ($<w'T'>$, the middle row, in unit of $Km^{-2}s^{-1}$) and turbulent flux of specific humidity ($<w'q'>$, the bottom row, in unit of $kg/kg\ m^{-2}s^{-1}$) from two air-sea coupled GFDL model simulations initialized identically that are run with (right column) and without (left column) the sea spray scheme. These fields are defined at the lowest model level (~35 m above the surface) and valid at 72 h into the model integration. The contour intervals for u*, $<w'T'>$ and $<w'q'>$ are 2 ms^{-1}, 0.1 $Km^{-2}s^{-1}$ and 0.0002 $kg/kg\ m^{-2}s^{-1}$, respectively.

As shown in Fig. 25, Bao *et al.* (2010) have done a study of sensitivity of the hurricane WRF model to a new spray parameterization that incorporates both momentum and

34

thermodynamic effects. This parameterization has now been implemented and tested in the GFDL coupled atmosphere-wave-ocean hurricane model. The scheme predicts that the overall impact of sea-spray droplets on the mean winds depends on the wind speed at the level of sea-spray generation. As the wind speed increases, the droplet size increases and the overall wind speed in the surface layer above the level of sea-spray generation increases, indicating that the increase of droplet size due to the increase of wind speed enhances the vertical mixing. This is consistent with observations and results from wind velocities that increase the overall enthalpy flux in the storm inner core shown in Fig. 25.

1.3.5 Summary

Significant progress has been made in understanding the basic oceanic and atmospheric processes that occur during TC passage over the last decade. The need is to isolate fundamental physical processes involved in the interactions through detailed process studies using experimental, empirical, theoretical, and numerical approaches. As demonstrated from new measurements, these approaches are needed to improve predictions of TC intensity and structure.

Considerable ocean-atmosphere variability occurs over the storm scales that include fundamental length scales such as the radius of maximum winds and another scale that includes the radius to gale-force winds. Here, the fundamental science questions are how the two fluids are coupled through OML and ABL processes, and what are the fundamental time scales of this interaction? These questions are not easily answered as the interactions must be occurring over various time/space scales. For example, one school of thought is that the only important process with respect to the ocean is under the eyewall where ocean cooling has occurred. While it is at the eyewall where the maximum wind and enthalpy fluxes occur, the broad surface circulation over the warm OML also has non-zero fluxes that are contributing thermal energy to the TC. The deeper the OML (and 26°C isotherm depth), more heat (OHC) is available to the storm through the enthalpy fluxes. Notwithstanding, it is not just the magnitude of the OHC, since the depth of the warm water is important to sustaining surface enthalpy fluxes. Process studies need to begin to look at these multiple scale aspects associated with the atmospheric response to ocean forcing.

With regard to the oceanic response to the atmospheric forcing, an important missing ingredient in many studies is the role of the forced and background current fields. In addition to aircraft-based sampling by AXCPs and AXCTDs and new profiling floats such as the EMAPEX and the SOLO (during CBLAST), efforts along the southeastern United States are underway to deploy long-range, HF-radars to map the surface currents to 200 km from the coast as part of an integrated ocean observing system. Such measurements would not only be invaluable to map the wind-driven surface currents during high winds, but also in the case of phased arrays, to map the directional wave spectra over the domain. These measurements could then be used to not only examine air-sea interactions, but also assess the relative importance of surface wave-current interactions under strong wind conditions in an Eulerian frame of reference.

The variability of the surface drag coefficient has received considerable attention over the last five years including the Coupled Boundary Layer an Air-Sea Transfer (CBLAST) program sponsored by the Office of Naval Research. Several treatments have come to the conclusion that there is a leveling off or a saturation values at about 30 m s^{-1} +/- 3 m s^{-1}. The ratio of the enthalpy coefficient and the drag coefficient is central to air sea fluxes impacting the TC boundary layer. In this context, the relationship between the coupled processes such as wave breaking and the generation of sea spray and how this is linked to localized air-sea fluxes remains a fertile research area. A key element of this topic is the atmospheric response to the oceanic forcing where there seems to be contrasting viewpoints. One argument is that the air-sea interactions are occurring over surface wave (wind-wave) time and space scales and cause significant intensity changes by more than a category due to very large surface drag coefficients. Yet empirical studies suggest the values to be between 2.5 to 3.4 x 10^{-3} compared to recent coupled model studies. While, these sub-mesoscale phenomena may affect the enthalpy fluxes, the first-order balances are primarily between the atmospheric and oceanic mixed layers.

1.3.6 Recommendations

The recommendations are:

i.) Given the range of uncertainty in the surface drag (e.g., wave effects), heat fluxes (e.g., sea spray), and initial conditions (e.g., wind field) beyond 30 m s^{-1}, assess how these combined uncertainties propagate through the coupled ocean-hurricane model;

ii.) Develop an archive of data sets and model outputs and make these archives publicly available for research and operational purposes. Investigate the potential use of these data sets in assimilation, evaluation, and verification of ocean models and parameterization schemes;

iii.) Create an *in-situ* tropical cyclone ocean-atmosphere observing program for pre-storm, storm, and post-storm environments. Develop optimal observing strategies and observational mixes for spatial evolution of upper ocean, interface, and atmospheric fields (including secondary circulations); and;

iv.) Develop improved ocean model initialization schemes through data assimilation of satellite and in situ measurements, and test mixing parameterizations for a spectrum of ocean, wave and atmospheric conditions including the impact of waves on the surface heat, moisture, and momentum fluxes, and thus on the evolving OML.

A common theme is that international research and forecasting programs need to build on recent field programs (ONR-CBLAST, NSF-sponsored measurements on Hurricane Isidore and Lili; IFEX and MMS Loop Current Dynamics Study, ONR ITOP) and acquire *in situ* data over a broad spectrum of atmospheric and oceanographic forcing regimes. These data are needed to test models and examine the parameter space in these air-sea interaction and vertical mixing schemes. Ultimately, future research initiatives must now

have strong experimental, empirical, analytical, and numerical modeling components to further our understanding of these complex coupling processes between these two fluids.

References:

Ali, M. M., P. S. V. Jagadeesh, and S. Jain, 2007: Effects of eddies on Bay of Bengal cyclone intensity, *EOS,* **88**, 93,95.

Andreas, E.L, 2010: Spray-mediated enthalpy flux to the atmosphere and salt flux to the ocean in high winds. *J. Phys. Oceanogr.*, **40**, 608-619.

Bao, J.-W., J. M. Wilczak, J. K. Choi, and L. H. Kantha, 2000: Numerical simulations of air-sea interaction under high wind conditions using a coupled model: A study of hurricane development. *Mon. Wea. Rev.*, **128**, 2190-2210.

Bao, J.-W., C. W. Fairall, S. A. Michelson, and L. Bianco, 2010: Parameterizations of sea-spray impact on the air-sea momentum and heat fluxes. *Mon. Wea. Rev.*, to appear.

Bender, M. and I. Ginis, 2000: Real-time simulation of hurricane-ocean interaction. *Mon. Wea. Rev.*, **128,** 917-946.

Bianco, L., J.-W. Bao, C. W. Fairall, and S. A. Michelson, 2010: Impact of sea spray on the surface boundary layer. *Mon. Wea. Rev.*, submitted.

Bister, M., and K. A. Emanuel, 1998: Dissipative heating and hurricane intensity. *Meteor. Atmos. Phys.,* **65**, 233–240.

Black, P. G., E. A. D'Asaro, W. Drennan, J. R. French, P. P. Niiler, T. B. Sanford, E. J. Terrill, E. J. Walsh, and J. Zhang, 2007: Air-sea exchange in hurricanes: synthesis of observations from the Coupled Boundary Layer Air-Sea Transfer experiment. *BAMS,* **88**, 357-384.

Bosart, L., C.S. Veldon, W.E. Bracken, J.Molinari, and P.G.Black, 2000: Environmental influences on the rapid intensification of hurricane Opal (1995) over the Gulf of Mexico. *Mon. Wea. Rev.*, **128**, 322-352.

Brassington, G. B., T. Pugh, C. Spillman, E. Schulz, H. Beggs, A. Schiller and P. R. Oke, 2007: BLUElink: Development of operational oceanography and servicing in Australia. *Journal of Research and Practice in Information Technology* **39,** 151-164.

Braun, S. A. and W.-K. Tao, 2000: Sensitivity of high resolution simulations of hurricane Bob (1991) to planetary boundary layer paramterizations. *Mon. Wea. Rev.*, **128**, 3941-3961.
Chan, J.C.L., Y. Duan and L.K. Shay. 2001: Tropical cyclone intensity change from a simple ocean-atmospheric coupled model. *J. Atmos. Sci.*, **58**, 154-172.

Chang, S., and R. Anthes, 1978: Numerical simulations of the ocean's nonlinear baroclinic response to translating hurricanes. *J. Phys. Oceanogr.*, **8**, 468-480.

Charnock, H., 1955: Wind stress on a water surface. *Quart. J. Royal Meteor. Soc.*, 639-640.

Chassignet, E. P., L. Smith, G. R. Halliwell, and R. Bleck, 2003: North Atlantic simulations with the hybrid coordinate ocean model (HYCOM): Impact of the vertical coordinate choice and resolution, reference density, and thermobaricity. *J. Phys. Oceanogr.*, **33**, 2504-2526.

Chen, S., J. F. Price, W. Zhao, M. Donelan, and E. J. Walsh, 2007: The CBLAST Hurricane program and the next generation fully coupled atmosphere-wave-ocean models for hurricane research and prediction., *BAMS*, **88**, 311-317.

Chen, S., T. J. Campbell, H. Jin, S. Gaberšek, R. M. Hodur and P. Martin, 2010: Effect of two-way air-sea coupling in high and low wind speed regimes. *Mon. Wea. Rev.*, In Press.

Cheney, R., L. Miller, R. Agreen, N. Doyle, and J. Lillibridge, 1994:, TOPEX/Poseidon: The 2-cm solution. *J. Geophys. Res.*, **99,** 24,555-24,563.

Church, J.A., T.M. Joyce, and J.F. Price, 1989: Current and density observation across the wake of Hurricane Gay, *J. Phys. Oceanogr.*, **19**, 259-265.

Cione, J.J., P. G. Black, S. H. Houston, 2000: Surface observations in the hurricane environment. *Mon. Wea. Rev*. **128**, 1550-1561.

Cione, J.J., and E.W. Uhlhorn, 2003: Sea surface temperature variability in hurricanes: Implications with respect to intensity change. *Mon. Wea. Rev*., **131**, 1783-1796.

Cooper, M., and K. Haines, 1996: Altimetric assimilation with water conservation properties. *J. Geophys. Res*., **101**, 1059-1077.

Cummings, J. A, 2003: Ocean data assimilation, *In* COAMPS: Version 3 Model Description, NRL Publication *NRL/PU/7500-03-448*. Naval Research Laboratory, Washington, DC, 20375, 21-28.

Dare, R. A. and N. E. Davidson, 2004: Characteristics of Tropical Cyclones in the Australian Region. *Monthly Weather Review* **132**, 3049-3065.

D'Asaro, E. A., 2003: The ocean boundary layer under hurricane Dennis. *J. Phys. Oceanogr*., **33**, 561-579.

D'Asaro, E. A., T. B. Sanford, E. Terrill, and P. Niiler, 2007: Cold wake of hurricane Francis, *Geophys Res. Lett.*, 34, L15609, doi:10.1029/2007GL030160, 6 pp.

DeCosmo, J. B., K. B. Katsaros, S. D. Smith, R. J. Anderson, W. A. Oost, K. Bumke, and H. Chadwick, 1996: Air-sea exchange of water vapor and sensible heat: The Humidity Exchange over the Sea (HEXOS) results. *J. Geophys. Res.*, **101**, 12,001-12,016.

DeMaria, M., M. Mainelli, L. K. Shay, J. Knaff, and J. Kaplan, 2005: Further improvements to the statistical hurricane intensity prediction scheme. *Wea and Forecasting,* **20**, 531-543.

Donelan, M A., 1990: Air-sea interaction. The Sea, B. LeMehaute abnd D. Hanes, Eds, *Ocean Engineering Science*, **9**, John Wiley and Sons, 239-292.

Donelan, M. A., B. K. Haus, N. Reul, W. J. Plant, M. Stiassine, H. Graber, O. Brown, and E. Saltzman, 2004: On the limiting aerodynamic roughness of the ocean in very strong winds. *Geophys. Res. Letters*., 31L18306,doi:1029/2004GRL019460.

Drennan, W. M. and L. K. Shay. 2006: On the variability of the fluxes of momentum and sensible heat. *Bound. Layer Meteor.,* **119(1)**, 81-107.

Drennan, W. M., J. A. Zhang, J. R. French, C. McCormick, and P. G. Black, 2007: Turbulent fluxes in the hurricane boundary layer, Part II: Latent heat flux. *J. Atmos. Sci.,* **64,** 1103- 1115.

Elliot, B. A., 1982: Anticyclonic rings in the Gulf of Mexico, *J. Phys. Oceanogr.,* **12**, 1292-1309.

Emanuel, K A., 1986: An air-sea interaction theory for tropical cyclones Part 1: Steady-State maintenance**.** *J. Atmos. Sci.***, 43,** 585-605.

Emanuel, K A., 1995: Sensitivity of tropical cyclones to surface exchange and a revised steady-state model incorporating eye dynamics**.** *J. Atmos. Sci.* **, 52,** 3969-3976.

Emanuel, K.A., 2003: A similarity hypothesis for air-sea exchange at extreme wind speeds. *J. Atmos. Sci.,* **60**, 1420-1428.

Faber, T., L. K. Shay, S. D. Jacob, S. H. Houston, and P. G. Black, 1997: Observed air-sea interactions during hurricane Emily. Preprints, *22ⁿᵈ Conf. on Hurricanes and Tropical Meteorology*, Fort Collins, CO, Amer. Meteor. Soc., 433-434.

Fairall, C.W., M. Banner, W. Peirson, R. P. Morison, and W. Asher, 2009: Investigation of the physical scaling of sea spray spume droplet production. *J. Geophys., Res*., **114**, C10001, doi:10.1029/2008JC004918.

Falkovich, A., I. Ginis, and S. Lord, 2005: Implementation of data assimilation and ocean initialization for the coupled GFDL/URI hurricane prediction system. *J. Atmos. and Ocean. Tech*., **22**, 1918–1932.

Findlater, J., 1969: A major low-level air current near the Indian Ocean during the northern summer. *Quart. J. R. Met. Soc*., **95,** 362-380.

Fox, D. N., W. J. Teague, C. N. Barron, M. R. Carnes, and C. M. Lee, 2002: The Modular Ocean Data Assimilation System (MODAS). *J. Atmos. Oceanogr. Tech.*, **19**, 240-252.

French, J. R., W. M. Drennan, J. A. Zhang, and P. G. Black, 2007: Turbulent fluxes in the hurricane boundary layer. Part 1: Momentum flux. *J. Atmos. Sci.*, **64,** 1089-1102.

Gaspar, P., 1988: Modeling the seasonal cycle of the upper ocean. *J. Phys. Oceanogr*., **18**, 161-180.

Geisler, J. E., 1970: Linear theory on the response of a two layer ocean to a moving hurricane. *Geophys. Fluid Dyn.*, **1**, 249-272.

Gill, A. E., 1984: On the behavior of internal waves in the wakes of storms. *J. Phys. Oceanogr.*, **14**, 1129-1151.

Ginis, I., 1995: Interaction of tropical cyclones with the ocean. *In Global Perspective of Tropical Cyclones,* Chapter 5, Ed. R. L. Elsberry, **Tech. Document WMO/TD 693**, World Meteorological Organization, Geneva, Switzerland, 198-260.

Goni, G. J., S. Kamholz, S. L. Garzoli, and D. B. Olson, 1996: Dynamics of the Brazil/Malvinas confluence based on inverted echo sounders and altimetry. *J. Geophys. Res.*, **95,** 22103-22120.

Greatbatch, R.J., 1983: On the response of the ocean to a moving storm: nonlinear dynamics. *J. Phys. Oceanogr.*, **13**, 357-367.

Halliwell, G., L. K. Shay, S. D. Jacob, O. Smedstad, and E. Uhlhorn, 2008: Improving ocean model initialization for coupled tropical cyclone forecast models using GODAE nowcasts. *Mon Wea Rev,* **136 (7)**, 2576–2591.

Halliwell, G., L. K. Shay, J. Brewster, and W. Teague, 2010: Evaluation and sensitivity analysis of an ocean model to hurricane Ivan in the northern Gulf of Mexico. *Mon. Wea. Rev*. **(In Press)**

Hanshaw, M. N., M. S. Lozier, and J. B. Palter, 2008: Integrated impact of tropical cyclones on sea surface cholophyll in the North Atlantic. *Geophys. Res. Lett.*, **35**, L01601 doi:10.1029/3007 GL031862.

Hara, T., and S. E. Belcher, 2004: Wind profile and drag coefficient over mature ocean surface wave spectra. *J. Phys. Oceanogr.*, **34,** 2345-2358.

Hock, T. J., and J. L. Franklin, 1999: The NCAR GPS dropwindsonde. *BAMS*, **80**, 407-420.

Ho, C.-R., Q. Zheng, Z.-W. Zheng, N.-J. Kuo, C.-K. Tai, and F.-C. Su, 2009:Reply to comment by A. Wada et al. on "Importance of pre-existing oceanic conditions to upper ocean response induced by Super Typhoon Hai-Tang", *Geophys. Res. Lett.*, 36, L09604.

Hong, X., S. W. Chang, S. Raman, L. K. Shay, and R. Hodur, 2000: The interaction of hurricane Opal (1995) and a warm core ring in the Gulf of Mexico. *Mon. Wea. Rev*., **128,** 1347-1365.

Innocentini, V., and I.A. Goncalves, 2010: The impact of spume droplets and wave stress parameterizations on simulated near-surface maritime wind and temperature. *J. Phys. Oceanogr.*, **40**, 1373-1389.

Jacob, D. S., L. K. Shay, A. J. Mariano, and P. G. Black, 2000: The three-dimensional mixed layer heat balance during hurricane Gilbert. *J. Phys. Oceanogr.*, **30**, 1407-1429.

Jacob, S. D., and L. K. Shay, 2003: The role of oceanic mesoscale features on the tropical cyclone-induced mixed layer response. *J. Phys. Oceanogr.*, **33**, 649-676.

Jacob, S. D., and C. Koblinsky, 2007: Effects of precipitation on the upper ocean response to a hurricane. *Mon Wea. Rev.,***135**, 2207-2225.

Jaimes, B. and L. K. Shay. 2009: Mixed layer cooling in mesoscale eddies during Katrina and Rita. *Mon. Wea. Rev*.**, 137(12)**, 4188-4207.

Jaimes, B. and L. K. Shay. 2010: Near-inertial wave wake of hurricanes Katrina and Rita in mesoscale eddies. *J. Phys. Oceanogr.*. **40(6),** 1320-1337.

Jarosz, E., D.A. Mitchell, D.W. Wang, and W.J. Teague, 2007: Bottom-up determination of air-sea momentum exchange under a major tropical cyclone. *Science*, **315**, 1707.

Jena, B., M. V. Rao and B. K. Sahu, 2006: TRMM-derived sea surface temperature in the wake of a cyclonic storm over the central Bay of Bengal. *Inter. J. of Rem. Sens.*, **27(14),** 3065-3072.

Jin, Y., W. T. Thompson, S. Wang, and C.-S. Liou, 2007: A numerical study of the effect of dissipative heating on tropical cyclone intensity. *Wea. Forecasting,* **22,** 950-966.

Kihara, N. and H. Hirakuchi, 2008: A model for air–sea interaction bulk coefficient over a warm mature sea under strong wind. *J. Phys. Oceanogr.*, **38**, 1313-1326.

Kitaigorodskii, S.A., 1968: On the calculation of the aerodynamic roughness of the sea surface. Izvestia. Acad. Sci. USSR, *Atmos. Oceanic Phys.*, **4**, 498-502.

Kraus, E.B. and J.S. Turner, 1967: A one-dimensional model of the seasonal thermocline. II: The general theory and its consequences. *Tellus*, **1**, 98-105.

Kudryavtsev, V. N., and V. K. Makin, 2009: Model of the spume sea spray generation. *Geophys. Res. Lett.*, **36**, L06801, doi:10.1029/2008GL036871

Large, W.G., and S. Pond, 1981: Open ocean momentum flux measurements in moderate to strong winds. J. *Phys. Oceanogr.*, **11,** 324-336, 1981.

Large, W., S., J. C. McWilliams, and S. C. Doney, 1994: Oceanic vertical mixing: A review and a model with non-local boundary layer parameterization. *Rev. Geophys.*, **32,** 363-403.

Leaman, K. D., 1976: Observations of vertical polarization and energy flux of near-inertial waves. *J. Phys. Oceanogr.***, 6**, 894-908.

Leben, R. R., 2005: Altimeter derived Loop Current metrics. In *Circulation in the Gulf of Mexico: observations and models, Geophys. Monogr.*, **161**, Amer. Geophys. Union, 181-201.

Leipper, D., and D. Volgenau, 1972: Hurricane heat potential of the Gulf of Mexico. *J. Phys. Oceanogr.*, **2,** 218-224.

Lin, I.-I., C.-C. Wu, K. A. Emanuel, I.-H. Lee, C.-R. Wu, and I.-F. Pun, 2005: The interaction of supertyphoon Maemi (2003) with a warm ocean eddy. *Mon Wea. Rev.*, **133**, 2635-2649.

Lin, I-I., I.-F. Pun and C.-C. Wu, 2008: Upper ocean thermal structure and the western north Pacific Category 5 typhoons. Part I: Ocean features and category 5 typhoons' intensification. *Mon. Wea Rev.*, **136**, 3288-3306.

Lin, I-I., I.-F. Pun and C.-C. Wu, 2009a: Upper ocean thermal structure and the western north Pacific Category 5 typhoons. Part II: Dependence on translation speed. *Mon. Wea Rev.*, **137**, 3744-3757.

Lin, I-I, Chi-Hong Chen, I-F. Pun, W. Timothy Liu, and C.-C. Wu, 2009b: Warm ocean anomaly, air sea fluxes, and the rapid intensification of tropical cyclone Nargis (2008), *Geophys. Res. Lett,* **36**, L03817, doi:10.1029/2008GL035815.

Mainelli, M., M. DeMaria, L. K. Shay and G. Goni, 2008: Application of oceanic heat content estimation to operational forecasting of recent category 5 hurricanes. *Wea. and Forecast,* **23**, 3-16.

Marks, F., and L.K. Shay, 1998: Landfalling tropical cyclones: Forecast problems and associated research opportunities: Report of the 5th Prospectus Development Team to the U.S. Weather Research Program, *BAMS,* **79**, 305-323.

Mellor, G. L., and T. Yamada, 1982: Development of a turbulence closure model for geophysical fluid problems. *Rev. Geophys. and Space Phys.*, **20,** 851-875.

Meyers, P. C., L. K. Shay and J. K. Brewster, 2010: The Systematically Merged Atlantic Regional Temperature and Salinity (SMARTS) Climatology for satellite derived ocean thermal structure, *17th Conference on Satellite Meteorology and Oceanography*, 27 – 30 Sept 2010, Annapolis, MD .

Moon, I., I. Ginis, and T. Hara, 2004a: Effect of surface waves on Charnock coefficient under tropical cyclones. *Geophys. Res. Lett.*, **31**, L20302.

Moon I.-J., I. Ginis, and T. Hara, 2004b: Effect of surface waves on air–sea momentum exchange. II: Behavior of drag coefficient under tropical cyclones. *J. Atmos. Sci.*, *61,* 2334–2348.

Moon, I., I. Ginis, and T. Hara, 2004c: Effect of surface waves on Charnock coefficient under tropical cyclones. *Geophys. Res. Lett.*, **31**, L20302.

Mueller, J.A., and F. Veron, 2009: A sea-state dependent spume generation function. *J. Phys. Oceanogr*., **39,** 2363-2372.

Nemoto, K., T. Midorikawa, A. Wada, K. Ogawa, S. Takatani, H. Kimoto, M. Ishii, and H. Y. Inoue,2008: Continuous observations of atmospheric and oceanic CO_2 using the moored buoy in the East China Sea: Variations during the passage of typhoons. *Deep-Sea Res. II*, 542-553.

Nilsson, J., 1995: Energy flux from traveling hurricanes to the oceanic internal wave field. *J. Phys. Oceanogr.*, **25**, 558-573. 1995.

Noh, Y. and H. J. Kim, 1999: Simulations of temperature and turbulence structure of the oceanic boundary layer with the improved near-surface process. *J. Geophys. Res.*, **104**, 15621-15634.

Ocampo-Torres, F.J., M.A. Donelan, N. Merzi, and F. Jia, 1994: Laboratory measurements of mass transfer of carbon dioxide and water vapour for smooth and rough flow conditions. *Tellus*, **46B**, 16-32.

Oke, P. R., A. Schiller, D. A. Griffin and G. B. Brassington, 2005: Ensemble data assimilation for an eddy-resolving ocean model of the Australian region. *Quarterly Journal of the Royal Meteorological Society* **1,** 1-11.

Palmen, E., 1948: On the formation and structure of tropical cyclones. *Geophyisca,* **3**, 26-38.

Park, J., K.-A. Park, K. Kim, and Y.-H. Youn, 2005: Statistical analysis of upper ocean temperature response to typhoons from ARGO floats and satellite data. *IEEE*, 2564-2567.

Powell, M. D., and S. Houston, 1996: Hurricane Andrew's landfall in South Florida. Part II: surface wind fields. *Wea and Forecasting*., **11**, 329-349.

Powell, M.D., P.J. Vickery, and T.A. Reinhold, 2003: Reduced drag coefficient for high wind speeds in tropical cyclones. *Nature*, **422,** 279-283.

Price, J. F., 1981: Upper ocean response to a hurricane. *J. Phys. Oceanogr.*, **11**, 153–175.

Price, J. F., R. A. Weller, and R. Pinkel, 1986: Diurnal cycling: Observations and models of the upper ocean response to diurnal heating, cooling and wind-mixing. *J. Geophys. Res.,***7,** 8411-8427.

Price, J. F., T. B. Sanford, and G.Z. Forristall, 1994: Observations and simulations of the forced response to moving hurricanes. *J. Phys. Oceanogr.*, **24**, 233-260.

Pudov, V., and S. Petrichenko, 2000: Trail of a typhoon in the salinity field of the ocean upper layer. *Atmospheric and Ocean Physics (Izvestiya Acad. Sci.)*, **36**, 700-706.

Pun, I-F, I-I Lin, C. -R. Wu, D. -S. Ko, W. -T. Liu, 2007: Validation and Application of Altimetry-derived Upper Ocean Thermal Structure in the Western North Pacific Ocean for Typhoon Intensity Forecast. *IEEE Trans. Geosci. Rem. Sens*., **45**, 1616-1630.

Rao, R. R., 1984: A case study on the influence of the summer monsoonal vortex on the thermal structure of upper central Arabian Sea during the phase of the MONEX-79. *Deep-Sea Res.*, **31**, 1511-1521.

Rastigejev, Y. and Yuh-Lang Lin, 2010: A theoretical study of fine ocean spray on tropical cyclones. *J. Geophys. Res.*, submitted.

Rogers, R., S. Aberson, M. Black, P. Black, J. Cione, P. Dodge, J. Dunion, J. Gamache, J. Kaplan, M. Powell, L. K. Shay, N. Surgi, and E. Uhlhorn, 2006: The intensity forecasting experiment (IFEX), a NOAA multiple year field program for improving intensity forecasts. *BAMS,* **87(11),** 1523-1537

Sandery P. A., G. B Brassington, A. Craig and T. Pugh., 2010: Impacts of ocean-atmosphere coupling on tropical cyclone intensity change and ocean prediction in the Australian region, *Mon. Wea. Rev.*, **138**, 2074-2091.

Sanford, T.B., P.G. Black, J. Haustein, J.W. Feeney, G. Z. Forristall, and J.F. Price, 1987: Ocean response to a hurricane. Part I: Observations. *J. Phys. Oceanogr*., **17**, 2065-2083.

Sanford, T.B., J.H. Dunlap, J.A. Carlson, D.C. Webb and J. B. Girton, 2005: Autonomous velocity and density profiler: EM-APEX. Proceedings of the IEEE/OES 8th Working Conference on Current Measurement Technology, IEEE Cat No. 05CH37650, ISBN: 0-7803-8989-1, 152-156.

Sanford, T B., J. F. Price, J. Girton, and D. C. Webb, 2007: Highly resolved observations and simulations of the oceanic response to a hurricane. *Geophys. Res. Lett.*, **34,** L13604, 5 pp.

Schade, L., and K. Emanuel, 1999: The ocean's effect on the intensity of tropical cyclones: Results from a simple ocean-atmosphere model. *J. Atmos. Sci.*, **56**, 642-651.

Scharroo, R., W.H. Smith, and J.L. Lillibridge, 2005: Satellite altimetry and the intensification of Hurricane Katrina. *EOS,* **86,** 366-367.

Schiller, A., P. R. Oke, G. B. Brassington, M. Entel, R. Fiedler, D. A. Griffin and J. Mansbridge, 2008: Eddy-resolving ocean circulation in the Asian-Australian region inferred from an ocean reanalysis effort. *Prog. Oceanogr.* **76,** 335-365.

Shay, L.K., 2009: Upper Ocean Structure: a Revisit of the Response to Strong Forcing Events. In*: Encyclopedia of Ocean Sciences*, ed. John Steele, S.A. Thorpe, Karl Turekian and R. A. Weller, Elsevier Press International, Oxford, UK, 4619-4637, doi: 10.1016/B978-012374473-9.00628-7.

Shay, L. K., 2010: Air-sea interactions in tropical cyclones (Chapter 3). *In Global Perspectives of Tropical Cyclones:* 2nd Edition, World Scientific Publishing Company: Earth System Science Publication Series, London, UK, Edited by J. C. Chan and J. D. Kepert, pp 93-132.

Shay, L.K. and R.L. Elsberry, 1987: Near-inertial ocean current response to hurricane Frederic. *J. Phys. Oceanogr.*, **17**, 1249 – 1269.

Shay, L.K., P.G. Black, A.J. Mariano, J.D. Hawkins and R.L. Elsberry, 1992: Upper ocean response to hurricane Gilbert. *J. Geophys. Res.,* **97**, 20,227 - 20,248.

Shay, L.K., and S.W. Chang, 1997: Free surface effects on the near-inertial ocean current response to a hurricane: A revisit. *J. Phys. Oceanogr*., **27**, 23 - 39.

Shay, L. K., G. J. Goni, and P. G. Black, 2000: Effects of a warm oceanic feature on hurricane Opal. *Mon. Wea. Rev.,* **128**, 1366-1383.

Shay, L. K, and S. D. Jacob, 2006: Relationship between oceanic energy fluxes and surface winds during tropical cyclone passage (Chapter 5). Atmosphere-Ocean Interactions II, *Advances in Fluid Mechanics*. Ed. W. Perrie, WIT Press, Southampton, UK, 115-142.

Shay, L. K., and E. W. Uhlhorn, 2008: Loop Current response to Hurricanes Isidore and Lili. *Mon Wea. Rev.,* **136***,* 3248-3274 doi: 10.1175/2008MWR2169.

Shay, L. K., and J. Brewster. 2010: Eastern Pacific oceanic heat content estimation for hurricane forecasting. *Mon. Wea. Rev*, 138, 2110-2131**.**

Sjoberg, B., and A. Stigebrandt, 1992: Computations of the geographical distribution of the energy flux to mixing processes via internal tides and the associated vertical circulation in the ocean. Deep-Sea Res., **39**, 269-291.

Soloviev, A., and R. Lukas, 2010: Effects of bubbles and sea spray on air–sea exchange in hurricane conditions. *Bound.-Layer Meteorol.,* **136**, 365–376, DOI 10.1007/s10546-010-9505-0.

Sun, D..R. Gautam, G. Cervone, Z. Boyeyi, and M. Kaptos, 2006: Comment on Satellite altimetry and the intensification of Hurricane Katrina. *EOS*, **87(8),** 89

Sturges, W., and R. Leben, 2000: Frequency of ring separations from the Loop Current in the Gulf of Mexico: A revised estimate. *J. Phys. Oceanogr.*, **30,** 1814-1819.

Teague, W. J., M. J. Carron, and P. J. Hogan, 1990: A comparison between the generalized digital environmental model and Levitus climatologies. *J. Geophys. Res.*, **95**, 99-116.

Teague, W.J., E. Jarosz, M.R. Carnes, D.A. Mitchell, and P.J. Hogan, 2006: Low-frequency current variability observed at the shelfbreak in the northeastern Gulf of Mexico: May − October 2004. *Cont. Shelf Res.*, doi:10.1016/j.csr.2006.08.002.

Teague, W.J., E. Jarosz, D.W. Wang, and D.A. Mitchell, 2007: Observed oceanic response over the upper continental slope and outer shelf during Hurricane Ivan. *J. Phys. Oceanogr.*, **37**, 2181-2206.

Toba, Y., N. Iida, H. Kawamura *et al.,* 1990: The wave dependence of sea surface wind stress. *J. Phys. Oceanogr.* **20**, 705-721.

Tolman, H. L., 2002: User manual and system documentation of WAVEWATCH-III version 2.22. NOAA/NWS/NCEP/OMB Tech. Note 222, 133 pp.

Uhlhorn, E. W., 2008: Gulf of Mexico Loop Current mechanical energy and vorticity response to a tropical cyclone. *PhD Dissertation.* RSMAS, University of Miami, Miami, FL 33149, 148 pp.

Uhlhorn, E. W., P. G. Black, J. L. Franklin, M. Goodberlet, J. Carswell and A. S. Goldstein, 2007:Hurricane surface wind measurements from an operational stepped frequency microwave radiometer. *Mon. Wea. Rev.*, **135,** 3070-3085.

Wada, A., 2009: Idealized numerical experiments associated with the intensity and rapid intensification of stationary tropical cyclone-like vortex and its relation to initial sea surface temperature and vortex-induced sea-surface cooling, *J. Geophys. Res.*, 114, D18111.

Wada, A., and N. Usui, 2007: Importance of tropical cyclone heat potential for tropical cyclone intensity and intensification in the western north Pacific. *J. of Oceanography*, **63**, 427-447.

Wada, A. and J. C. L. Chan , 2008: Relationship between typhoon activity and upper ocean heat content. *Geophys. Res. Lett.,* **35**, L17603.

Wada, A., H. Niino and H. Nakano, 2009a: Roles of vertical turbulent mixing in the ocean response to Typhoon Rex (1998), *J. Oceanogr.*, **65**, 373-396.

Wada, A., K. Sato, N. Usui and Y. Kawai, 2009b: Comment on "The importance of pre-existing oceanic conditions to upper ocean response induced by Super Typhoon Hai-Tang" by Zheng Z.-W.C.-R. Ho and N.-J. Kuo. *Geophys. Res. Lett.*, **36**, L09603.

Wada, A, N. Kohno and Y. Kawai, 2010a: Impact of wave-ocean interaction on Typhoon Hai-Tang in 2005, *SOLA*, **6A**, 13-16.

Wada, A. and N. Usui, 2010b: Impacts of Oceanic Preexisting Conditions on Predictions of Typhoon Hai-Tang in 2005, *Advances in Meteorology*, 756071.

Walker, N., R. R. Leben, and S. Balasubramanian 2005: Hurricane forced upwelling and chlorophyll a enhancement within cold core cyclones in the Gulf of Mexico. *Geophys. Res. Letter,* **32**, L18610, doi: 10.1029/2005GL023716, 1-5.

Wang, B., and X. Zhou , 2008: Climate variation and prediction of rapid intensification in tropical cyclones in the western North Pacific, *Meteorol. Atmos. Phys.*, **99**, 1– 16.

Wang, D.W., D.A. Mitchell, W.J. Teague, E. Jarosz, and M.S. Hulbert, 2005: Extreme waves under Hurricane Ivan. *Science*, **309**, 896.

Wang, Y., J. D. Kepert, and G. J. Holland, 2001: The effect of sea spray evaporation on tropical cyclone boundary layer structure and intensity. *Mon. Wea. Rev*., **129**, 2481-2500.

Wright, C. W., E. J. Walsh, D. Vandemark, W. B. Krabill, A. W. Garcia, S. Houston, M. Powell, P. Black, and F. D. Marks, 2001: Hurricane directional wave spectrum spatial variations in the open ocean. *J. Phys. Oceanogr.,* **31**, 2472-2488.

Wu, C.-C., C.-Y. Lee, and I-I Lin, 2007: The effect of the ocean eddy on tropical cyclone intensity. *J. Atmos. Sci.,* **64(10)**, 3562-3578.

Yablonsky, R. M, and I. Ginis, 2009: Limitation of one-dimensional ocean models for coupled hurricane-ocean forecasts. *Mon. Wea. Rev*., DOI 10.1175/2009MWR2863

Yin, X., Z. Wang, Y. Liu, and Y. Xu., 2007: Ocean response to typhoon Ketsana traveling over the northwest Pacific and a numerical model approach. *Geophys. Res. Lett.*, **34**, doi:10.1029/3007GL031477.

Yoshikawa, Y., A. Masuda, K. Marbayashi, M. Ishibashi, and A. Okuno, 2006: On the accuracy of HF radar measurement in the Tsushima Strait, *J. Geophys. Res.*, **111**, C04009, doi:10.1029/2005JC003232.

Zedler, S., T. Dickey, S. Doney, J. Price, X. Yu, and G. Mellor, 2001: Analyses and simulations of the upper ocean's response to hurricane Felix at the Bermuda Testbed Mooring site: 13-23 August 1995. *J. Geophys. Res,* **107**, 3232.

Zhang, J. A., 2007: An airborne investigation of the atmospheric boundary layer structure in the hurricane force wind regime. *Ph.D.Dissertation*, RSMAS, University of Miami, Miami, FL 33149, 60pp.

Zhang, D.-L., and E. Altshuler, 1999: The effects of dissipative heating on hurricane intensity. *Mon. Wea. Rev.,* **127**, 3032–3038.

Zheng, Z.-W., C.-R. Ho, and N.-J. Kuo , 2008: Importance of pre-existing oceanic conditions to upper ocean response induced by super typhoon Hai-Tang. *Geophys. Res. Lett.*, 35, L20603.